RSC Advances

PAPER

View Article Online
View Journal | View Issue

Cite this: *RSC Adv.*, 2025, **15**, 49269

Study of the structural, optical and dielectric properties of the $Ba_{0.95}Sm_{0.034}Ti_{(1-x)}Zr_xO_3$ solid solution

El Hassan Yahakoub, *[a] Khalid Lemrini,[a] Talal Moudrikah,[a] El Houcine Lahrar,[b] Slimane Raissi,[c] Amine Bendahhou,[a] Ilyas Jalafi,[a] Fatima Chaou,[a] Soufian El Barkany[a] and Mohamed Abou-Salama[a]

The solid solution $Ba_{0.95}Sm_{0.034}Ti_{1-x}Zr_xO_3$, with $x = 0.01$, 0.05, and 0.10, was synthesized *via* the solid-state reaction method at 1200 °C for 6 h. The obtained powders were first characterized by X-ray diffraction (XRD) to confirm the formation of the expected phase. All samples were found to exhibit a tetragonal structure with space group *P*4*mm*, as determined by Rietveld refinement of the XRD data. Increasing the zirconium content led to an expansion of the unit cell volume and a distortion of the [Ti/ZrO_6] octahedra. Scanning electron microscopy (SEM) images of pellets sintered at 1300 °C for 6 h showed a denser microstructure with larger grains in Zr-rich ceramics. A significant modification of the optical bandgap energy was observed with increasing Zr content. Dielectric measurements showed that the Curie temperature gradually decreases with increasing zirconium content. The electrical properties were influenced by the contributions of grains and grain boundaries. The total electrical resistance ($R_{tot} = R_g + R_{gb}$) increased with the zirconium content. The analysis of the complex electrical modulus confirmed a non-Debye behavior for all the ceramics studied in this work.

Received 20th October 2025
Accepted 2nd December 2025

DOI: 10.1039/d5ra08059b

rsc.li/rsc-advances

1. Introduction

Future generations of advanced materials, such as humidity sensors, resonators, filters, capacitors, memory devices, and gas sensors, require materials with high potential. To meet the growing demands of modern electronics, researchers are actively exploring new dielectric materials that combine high permittivity with exceptional stability under frequency and temperature variations. The ABO_3 structure of the perovskite family is widely used in modern technologies due to its multifunctional properties, including piezoelectricity, ferroelectricity, multiferroicity, superconductivity, magneto-dielectric behavior, and energy storage capability.[1–6] Among these materials, barium titanate ($BaTiO_3$) has attracted significant interest since the discovery of Rochelle salt in 1921.[7] Due to its remarkable ferroelectric and relaxor-ferroelectric properties, it is a prime candidate for energy storage applications. Maintaining ferroelectric behavior at room temperature, along with improving the electrical and dielectric performance, represents a major focus of research. Despite the progress achieved through the partial substitution of Ti^{4+} by Zr^{4+} in the $BaTi_{1-x}Zr_xO_3$ system and the co-substitution of rare earth elements Re^{3+} and Zr^{4+} in the $Ba_{(1-x)}Re_xTi_{(1-y)}Zr_yO_3$ system, which have shown promising results, optimizing the concentrations of rare earth elements and zirconium in these systems remains a significant challenge, attracting sustained interest in this field.

The partial substitution of titanium by zirconium in barium titanate ($BaTiO_3$) enhances the materials piezoelectric, ferroelectric, and relaxor properties compared to pure $BaTiO_3$.[8] The gradual introduction of Zr into the $BaTiO_3$ structure leads to the formation of three distinct compositional domains within the $BaTi_{1-x}Zr_xO_3$ (BZT) solid solution, each characterized by specific dielectric responses and structural properties that depend on the zirconium content.[9–11] For x values between 0 and 0.15, the material exhibits a significantly higher dielectric constant compared to unmodified $BaTiO_3$. In the range $0.15 \leq x \leq 0.27$, a diffuse phase transition is observed, indicating a gradual change in ferroelectric behavior. As the zirconium content increases further ($0.27 \leq x \leq 0.40$), the BZT compound develops a typical relaxor behavior, resulting from the continuous evolution of the diffuse phase transition.[12] The polymorphic phase transitions identified in the BZT structure include successive transformations from rhombohedral to orthorhombic (T_1), orthorhombic to tetragonal (T_2), and finally

[a]*Department of Chemistry, Laboratory of Molecular Chemistry, Materials and Environment (LCM2E)-The Multidisciplinary Faculty of Nador, University Mohamed Premier, B.P. 300, Selouane, Nador 62700, Morocco. E-mail: elhassan.yahakoub@ump.ac.ma*

[b]*Laboratory of Inorganic Materials for Sustainable Energy Technologies (LIMSET), University Mohammed VI Polytechnic, Benguerir, 43150, Morocco*

[c]*PSL University, Chimie ParisTech–CNRS, Institut de Recherche de Chimie Paris, 11 rue Pierre et Marie Curie, Paris 75005, France*

from tetragonal to cubic at the curie temperature (T_C). These transitions tend to converge as the Zr content increases, resulting in a decrease in the T_C transition temperature, while the temperatures of the T_1 and T_2 transitions increase.[13,14] To further enhance the materials properties, other strategies include substituting barium with alkaline earth elements of the same valence, such as Ca^{2+} and Sr^{2+},[15–20] or with higher valence lanthanides such as La^{3+}, Sm^{3+}, Gd^{3+}, Nd^{3+},Pr^{3+}, Eu^{3+},[21–23] as well as other cations like Y^{3+}, Bi^{3+} or Sc^{3+}.[24–27] These approaches allow modulation of the electrical and dielectric properties while influencing the crystal structure and charge carrier mobility. Among these systems, the pseudo-binary system $(1-x)Ba(Zr_{0.2}Ti_{0.8})O_3$–$x(Ba_{0.7}Ca_{0.3})TiO_3$ (BCZT) has attracted considerable attention due to the presence of a morphotropic phase boundary (MPB) and a "convergence region", similar to those observed in the PZT and PMN-PT systems.[28,29] This system exhibits outstanding energy storage properties and also shows great potential for cooling applications.[30–32] Additionally, lanthanide modified BZT systems are attracting considerable interest because the introduction of higher valence ions such as La^{3+}, Sm^{3+}, Gd^{3+}, Eu^{3+} creates a charge imbalance that leads to the formation of cation vacancies (at the Ba site) or oxygen vacancies in order to maintain electrostatic neutrality.[27,33,34] These defects, together with the local lattice distortions induced by lanthanide ions, strongly affect charge-carrier mobility, electrical conductivity, and the dielectric and ferroelectric responses of the material. Altogether, these effects promote relaxor type behaviours and broaden the operational temperature range, which is particularly advantageous for high-performance applications.[14,23,33,35–37] The incorporation of rare-earth elements (Re^{3+}) at the A-site of the BZT system distorts the [Ti/ZrO_6] octahedra, modifying the lattice symmetry and affecting the grain size, a key parameter for structural and electrical properties.[14,33,35,38] This substitution also enhances the dielectric performance, as reported by Ostos *et al.*, increasing the dielectric constant and stabilizing the structure for La^{3+}, Nd^{3+}, and Pr^{3+}.[39] Furthermore, the optical properties of the BZT system are also affected by this type of substitution, particularly when Ba is replaced by Gd, resulting in a reduction of the band gap energy (E_{gap}).[36,40]

This study focuses on the synthesis and characterization of perovskite-structured materials, specifically the composition $Ba_{0.95}Sm_{0.034}Ti_{1-x}Zr_xO_3$, with the aim of optimizing the zirconium content while preserving ferroelectric behavior at room temperature. It seeks to address the following question: up to what zirconium content can titanium be substituted without compromising the room-temperature ferroelectricity, and how does this substitution affect the crystal structure, microstructure, as well as the dielectric, electrical, and optical properties of the synthesized material?

2. Synthesis and characterization

The $Ba_{0.95}Sm_{0.034}Ti_{(1-x)}Zr_xO_3$ powders, with $x = 0.01$, 0.05, and 0.10 (hereafter referred to as ZrSm0.01, ZrSm0.05, and ZrSm0.10), were synthesized using the conventional solid-state reaction method. The starting materials included $BaCO_3$ (Sigma-Aldrich, 99.9%), TiO_2 (Sigma-Aldrich, 99%), ZrO_2 (Sigma-Aldrich, 99%), and Sm_2O_3 (Sigma-Aldrich, 99.9%). Prior to mixing, samarium oxide (Sm_2O_3) was pre-calcined at 850 °C for 2 h after accurate weighing. The raw materials were weighed in stoichiometric proportions and ball-milled in ethanol for 12 h using zirconia balls. The resulting slurry was dried at 80 °C to remove residual moisture. The dry powders were then manually ground in an agate mortar for 30 minutes to ensure

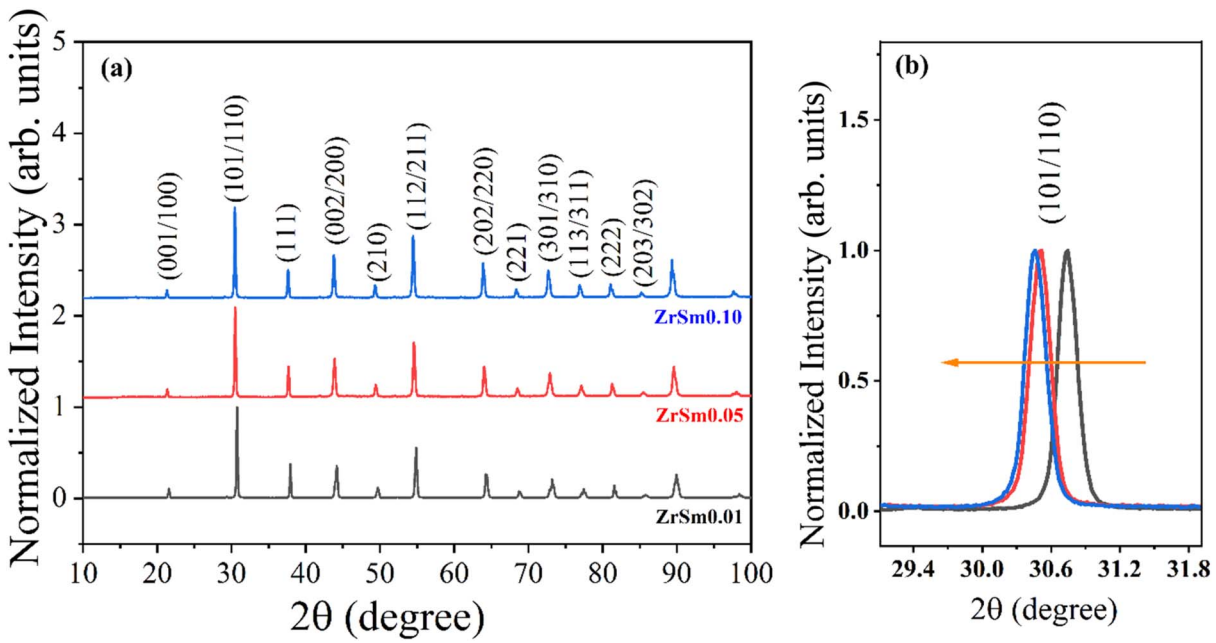

Fig. 1 (a) X-ray diffractograms of the ZrSm0.01, ZrSm0.05, and ZrSm0.10 ceramics. (b) Magnified view of the 2θ region between 29.4° and 31.8°.

uniform mixing. Calcination was carried out at 1200 °C for 6 h to promote solid state reactions. The resulting powders were mixed with a polyvinyl alcohol (PVA) binder and pressed under a uniaxial pressure of 20 kN to form cylindrical pellets. Sintering of the pellets was performed in air at 1300 °C for 6 h. The heating protocol included an initial increase in temperature to 700 °C at a rate of 10 °C min^{-1}, followed by maintaining this temperature for 1 h, followed by a second ramp to the sintering temperature at 5 °C min^{-1}. After sintering, the samples were cooled naturally to room temperature.

The crystal structure analysis of the ZrSm0.01, ZrSm0.05, and ZrSm0.10 powders by X-ray diffraction was performed using a D8 diffractometer (Bruker, Karlsruhe, Germany). The X-ray were generated by a copper anticathode ($CuK_{\alpha 1}$ with λ =

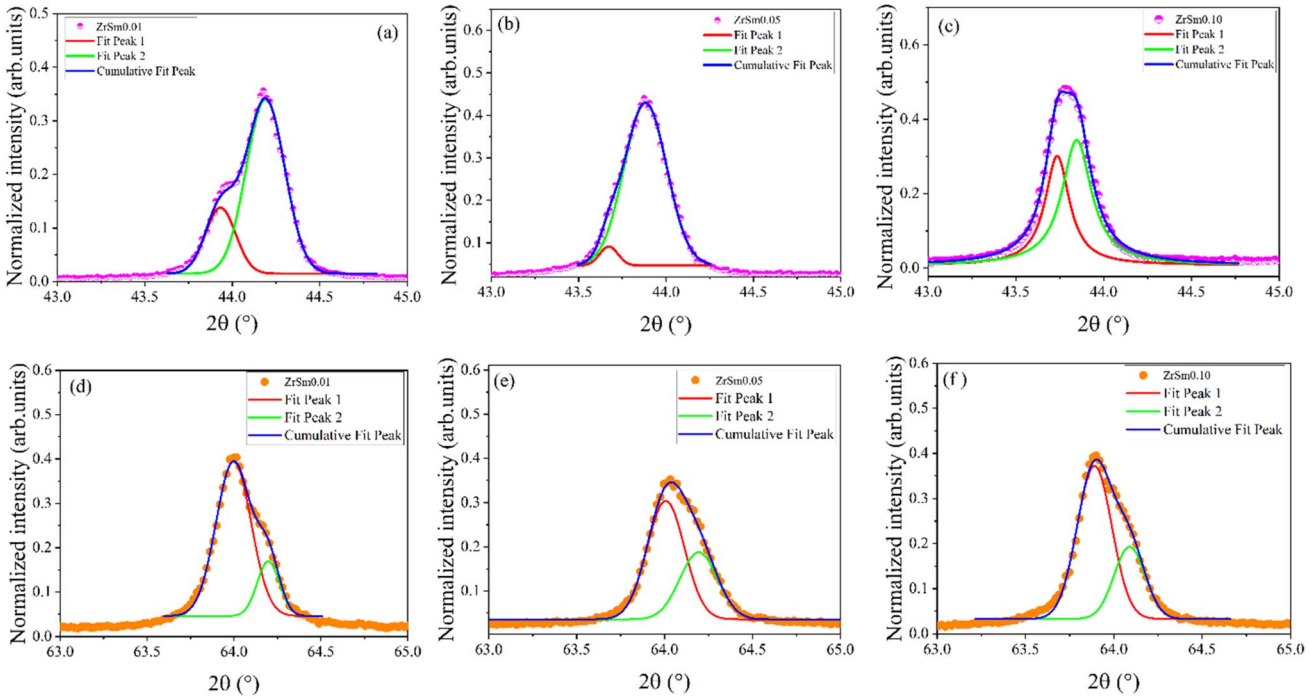

Fig. 2 (a), (b) and (c) show the diffraction peaks in the 45° region, while (d), (e), and (f) show the diffraction peaks in the 65° region for all compositions.

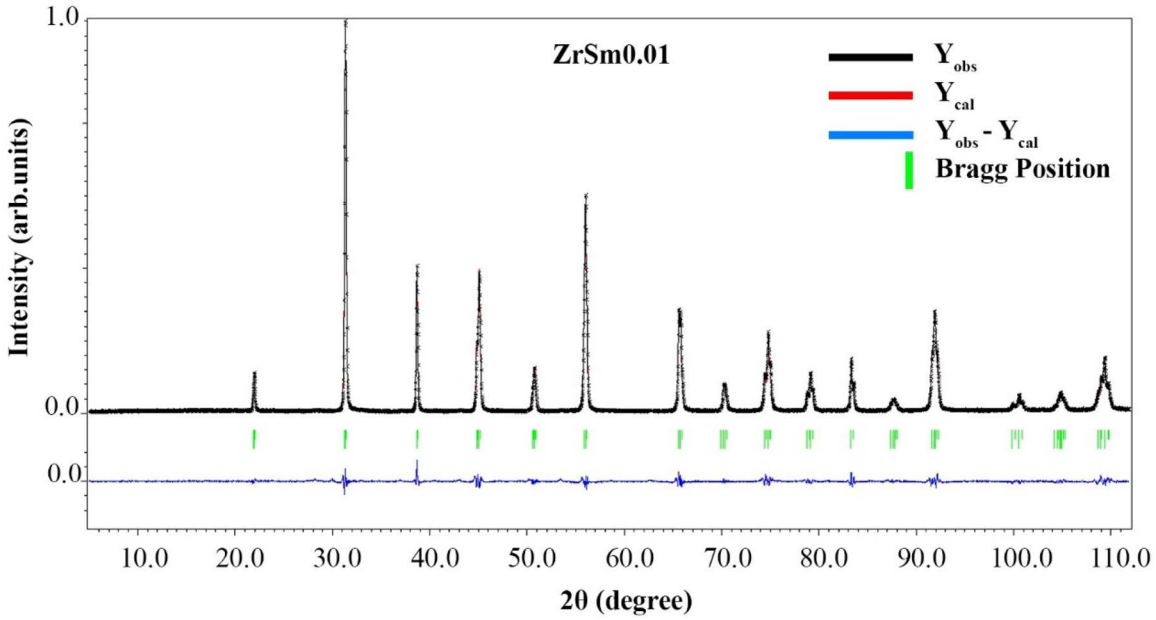

Fig. 3 Rietveld-refined XRD pattern of the ZrSm0.01 sample.

1.5406 Å and $CuK_{\alpha 2}$ with $\lambda = 1.54439$ Å), with a scanning speed of 0.012° per second at room temperature. Data acquisition was conducted at 40 kV and 40 mA. Rietveld refinement of the obtained data was performed using the Jana 2006 software.[41] After X-ray diffraction analysis, the sintered pellets were carefully polished to obtain parallel surfaces, then annealed at 300 °C for 30 min. The morphology of the ceramics was analyzed using scanning electron microscopy (SEM) with a TESCAN VEGA III LM microscope, operating at an accelerating voltage of 10 KV. Optical properties of the material were evaluated using a UV-Visible spectrophotometer (UV-Shimadzu). The pellets were coated with a thin layer of silver paste, then thermally treated at 300 °C for 30 minutes to improve adhesion, before being cooled down to room temperature. This step was carried out prior to analysis by complex impedance spectroscopy. Impedance spectroscopy was performed using a BioLogic MTZ-35 analyzer coupled with a temperature-controlled oven. Measurements were carried out over a frequency range from 10 Hz to 1 MHz, applying an AC signal with an amplitude of 1 V.

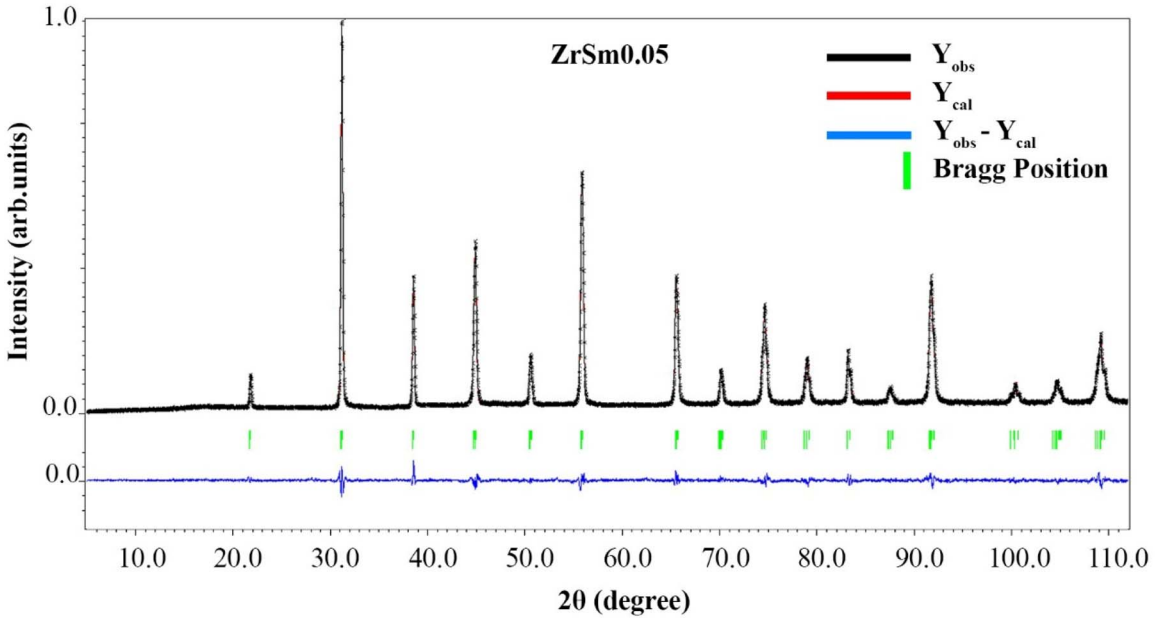

Fig. 4 Rietveld-refined XRD pattern of the ZrSm0.05 sample.

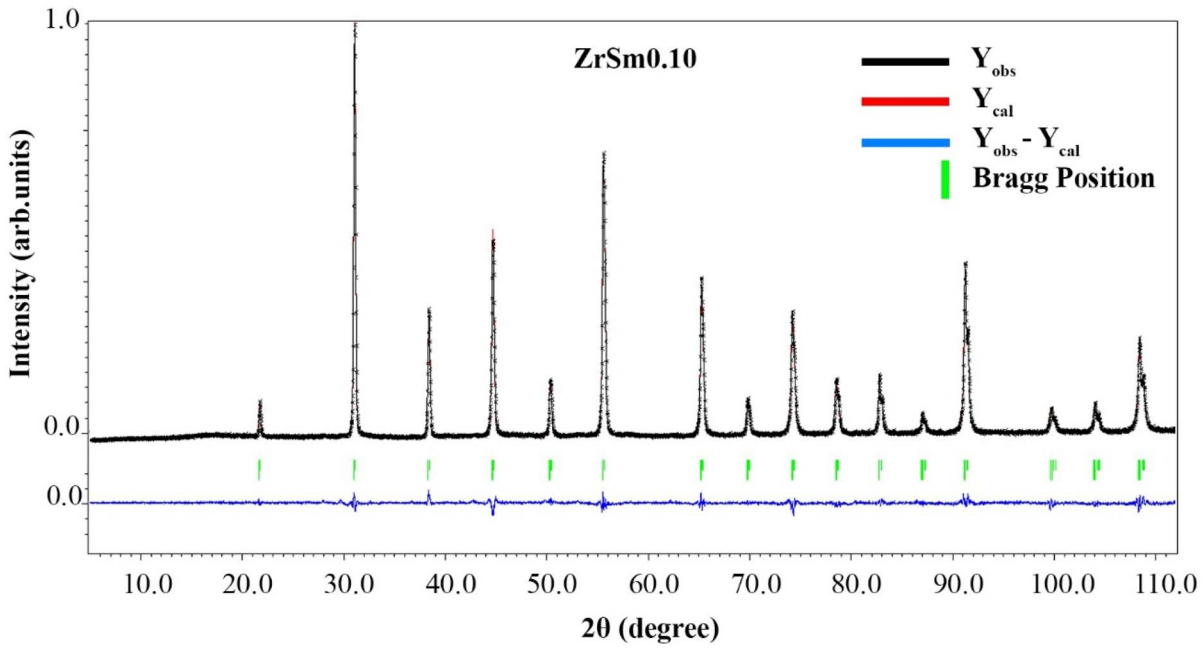

Fig. 5 Rietveld-refined XRD pattern of the ZrSm0.10 sample.

3. Results and discussion

3.1. X-ray diffraction analysis

The X-ray diffraction patterns of the $Ba_{0.95}Sm_{0.034}Ti_{(1-x)}Zr_xO_3$ solid solution powders, with $x = 0.01$, 0.05, and 0.10, are presented in Fig. 1(a). The peaks recorded at room temperature are sharp, confirming the good crystallinity of our powders. The most intense XRD peaks, observed around 32° and corresponding to the (101/110) plane, indicate the presence of the perovskite phase in all prepared compositions. The purity and tetragonal crystal structure of the obtained ceramics were confirmed using JCPDS No. 05-0626. All Bragg peaks can be fully indexed to the tetragonal structure of the $Ba_{0.95}Sr_{0.05}TiO_3$ phase.[42]

The most intense peak in the XRD spectra is observed around 31° in each sample, as shown in Fig. 1(b). It is clear that the diffraction peaks tend to shift towards lower 2θ values as the zirconium content increases. According to Bragg's law,[43] a decrease in the 2θ angle results in an increase in the crystal lattice volume. Indeed, the substitution of Ti^{4+} ($R_{Ti^{4+}} = 0.605$ Å) by Zr^{4+} ($R_{Zr^{4+}} = 0.72$ Å), due to the difference in ionic radii, induces a lattice expansion that may lead to an increase in the lattice parameters.[44]

To determine the structures or the phases present in the studied powders, peak deconvolution around 45° and 64°, as well as Rietveld refinement of the crystalline structures, were performed. For the reference structure of barium titanate, the diffraction peaks around 45° correspond to the (002)/(200)T reflections of the tetragonal phase, (200)/(022)O of the orthorhombic phase, (200)R of the rhombohedral phase, and (200)C of the cubic phase.[45] The diffraction peaks located between 43° and 45° have been magnified and presented in Fig. 2(a)–(c) for the three compounds studied. The presence of a doublet in this region for each compound clearly suggests the presence of a tetragonal phase (*P4mm*),[15] a peak corresponding to an orthorhombic phase (*Amm*2),[46] or a mixture of both phases. Furthermore, the orthorhombic phase (*Amm*2) exhibits a triplet around 65°,[10] corresponding to the (004), (040), and (222) reflections.[46] On the other hand, the tetragonal phase (*P4mm*) shows a doublet in this region, corresponding to the (202) and (220) reflections. A zoom on the peaks located between 63° and 65° in the diffractograms is illustrated in Fig. 2(d)–(f). The presence of a doublet in this region, associated with the (202) and (220) reflections, strongly suggests that our samples are crystallized in the tetragonal phase (*P4mm*).

To confirm the presence of the tetragonal phase in our ceramics, we performed a refinement using the Rietveld method, adopting an initial model based on a classic tetragonal perovskite structure with the formula $Ba_{0.95}Sr_{0.05}TiO_3$, belonging to the *P4mm* space group, with lattice parameters $a = 3.989$ Å and $c = 4.026$ Å.[47] In this model, Ba/Re atoms occupy the 1a site (0.5, 0.5, z), while Ti/Zr are located at the 1b site (0, 0, z). As established for the $Ba_{0.95}Sr_{0.05}TiO_3$ structure, oxygen occupies two crystallographic ally distinct positions: the 1c site (0.5, 0, z) assigned to O1 and the 1d site (0, 0, z) assigned to O2.

Fig. 3, 4 and 5 show the Rietveld refinement spectra for all the studied compounds. The experimental XRD spectra and the calculated models exhibit good agreement for all compositions refined using the Rietveld method, confirming that all

Table 1 Rietveld refinement results of the XRD spectra for the $Ba_{0.95}Sm_{0.034}Ti_{(1-x)}Zr_xO_3$ composition

Compounds	ZrSm0.01	ZrSm0.05	ZrSm0.10
a (Å)	4.0015 (3)	4.00971 (5)	4.01947 (17)
c (Å)	4.0196 (5)	4.02287 (8)	4.02462 (14)
c/a	1.0051	1.0033	1.0013
V (Å^3)	64.0394 (11)	64.6787 (18)	65.1060 (4)
R_p (%)	7.27	5.33	5.63
R_{wp} (%)	10.45	6.99	7.51
R_{exp} (%)	6.09	4.98	5.39
GOF	1.72	1.40	1.39

Table 3 Selected bond lengths (Å) for $Ba_{0.95}Sm_{0.034}Ti_{(1-x)}Zr_xO_3$

Bond distances (Å)	ZrSm0.01	ZrSm0.05	ZrSm0.10
4(Ti/Zr–O1)	2.00131 (0)	2.00753 (3)	2.02459 (7)
1(Ti/Zr–O2)	2.13438 (3)	2.11650 (5)	2.01682 (9)
1(Ti/Zr–O2)	1.88758 (3)	1.90637 (4)	2.00265 (9)
4(Ba/Ln–O1)	2.82003 (2)	2.77236 (4)	2.75319 (8)
4(Ba/Ln–O1)	2.85349 (2)	2.90918 (4)	2.93785 (9)
4(Ba/Ln–O2)	2.83117 (3)	2.83699 (4)	2.84756 (10)

Table 2 Refined structural parameters for the $Ba_{0.95}Sm_{0.034}Ti_{(1-x)}Zr_xO_3$ powder from X-ray diffraction data

Compounds	Atoms	x	y	z	U_{iso} (Å)	Wyckoff position	Site occupancy
ZrSm0.01	Ba/Sm	0.5	0.5	0.5162 (12)	0.0112 (5)	1a	0.95/0.034
	Ti/Zr	0	0	0.022 (4)	0.0123 (6)	1b	0.99/0.01
	O1	0.5	0	0.010 (17)	0.0160 (11)	1c	1
	O2	0	0	0.492 (5)	0.0160 (11)	1d	1
ZrSm0.05	Ba/Sm	0.5	0.5	0.5175 (14)	0.0186 (14)	1a	0.95/0.034
	Ti/Zr	0	0	0.016 (5)	0.0170 (13)	1b	0.95/0.05
	O1	0.5	0	0.042 (6)	0.018 (18)	1c	1
	O2	0	0	0.542 (7)	0.018 (18)	1d	1
ZrSm0.1	Ba/Sm	0.5	0.5	0.5184 (7)	0.0139 (5)	1a	0.95/0.034
	Ti/Zr	0	0	0.041 (2)	0.0118 (10)	1b	0.90/0.10
	O1	0.5	0	−0.014 (4)	0.012 (2)	1c	1
	O2	0	0	0.543 (9)	0.012 (2)	1d	1

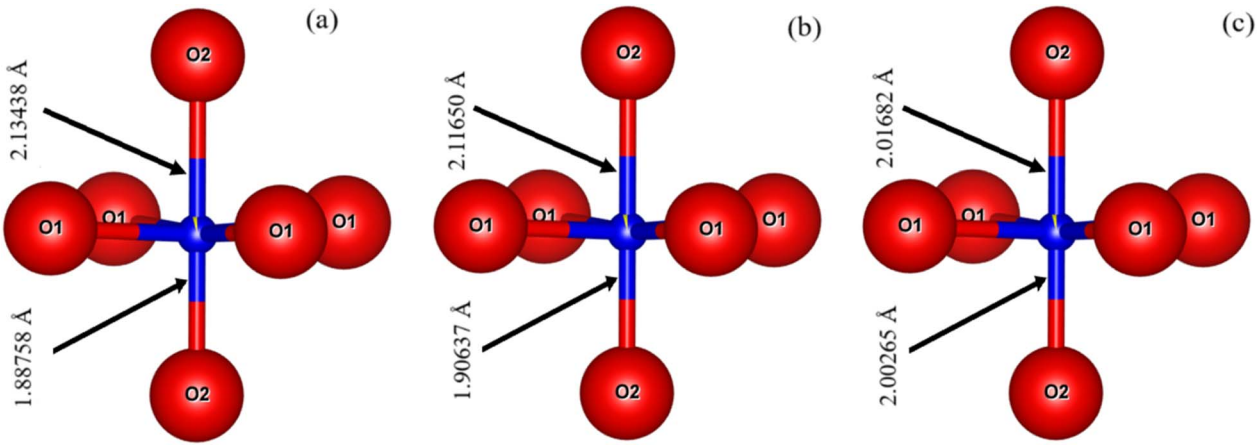

Fig. 6 Representation of [Ti/ZrO_6] octahedra for the ceramics (a) ZrSm0.01, (b) ZrSm0.05, and (c) ZrSm0.10.

synthesized materials adopt a tetragonal perovskite structure with the *P4mm* space group. The refinement results, including the lattice parameters (a, c, V) and reliability factors (R_p, R_{wp}, GOF), are summarized in Table 1.

Table 4 Theoretical, calculated, and relative densities of the studied ceramics

Compounds	ρ_m (g cm^{-3})	ρ_{th} (g cm^{-3})	ρ_r (%) $= \frac{\rho_m}{\rho_{th}} \times 100$
ZrSm0.01	5.5518	5.9796	92.84
ZrSm0.05	5.5853	5.9981	93.11
ZrSm0.10	5.6989	6.0141	94.76

According to the results presented in this table, we can observe that the lattice parameters a and c increase with the rising Zr content. Consequently, the unit cell volume expands, which is consistent with the shift of X-ray diffraction peaks toward lower 2θ values. This volume increase can be attributed to the substitution of Ti^{4+} ions by Zr^{4+} ions. Additionally, the tetragonality ratio c/a decreases as the Zr^{4+} concentration increases, indicating a reduction in tetragonality. The (002) and (200) diffraction peaks, located between 44° and 45° (see Fig. 2(a)–(c)) for the three studied compositions, reveal that the increase in Zr^{4+} content and the corresponding decrease in Ti^{4+} content at the B site led to the merging of these peaks. This clearly demonstrates that the tetragonality of the crystal structure decreases with increasing Zr^{4+} concentration.

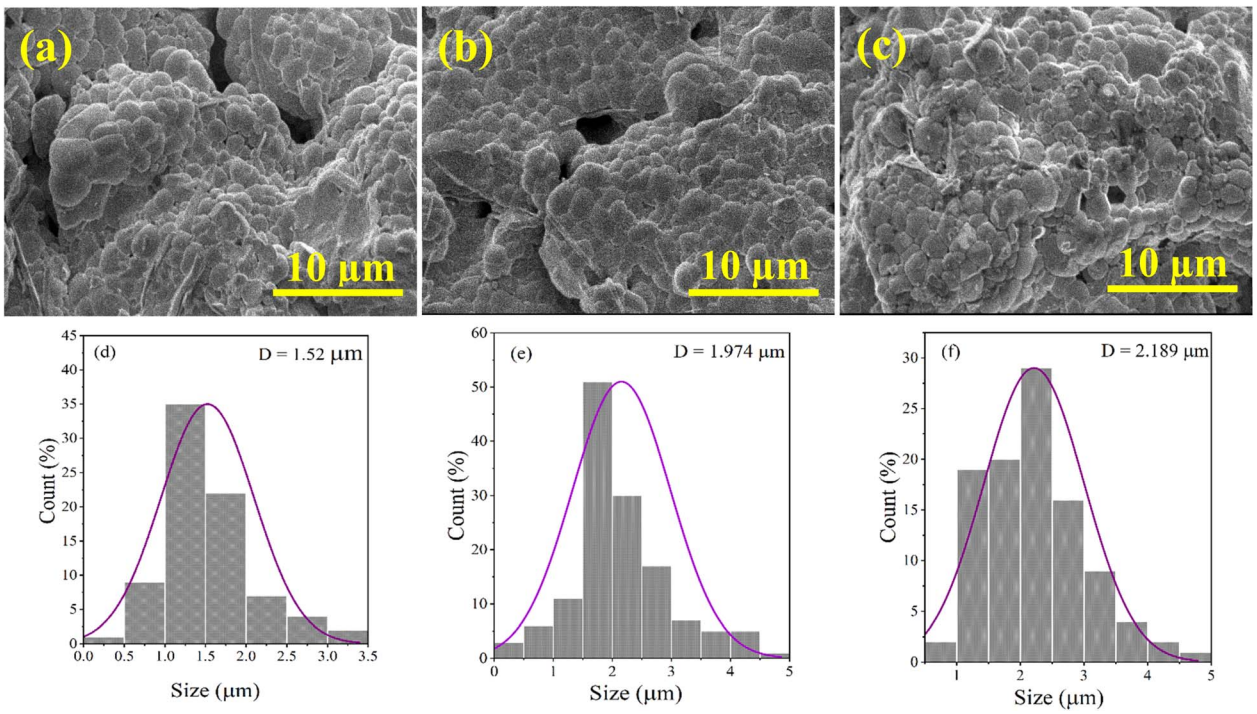

Fig. 7 (a), (b), and (c) are the SEM images, and (d), (e), and (f) are the histograms of the ZrSm0.01, ZrSm0.05, and ZrSm0.10.

The quality of the refinement was assessed based on the reliability *R*-factors. All synthesized materials exhibited satisfactory refinement, as evidenced by the low values of R_p, R_{wp}, R_{exp}, and the goodness-of-fit (GOF), as presented in Table 1. The crystallographic parameters obtained, such as the atomic positions, Wyckoff positions, and the isotropic thermal displacement factor (U_{iso}) for each atom, derived from the refinement for all compositions, are compiled in Table 2.

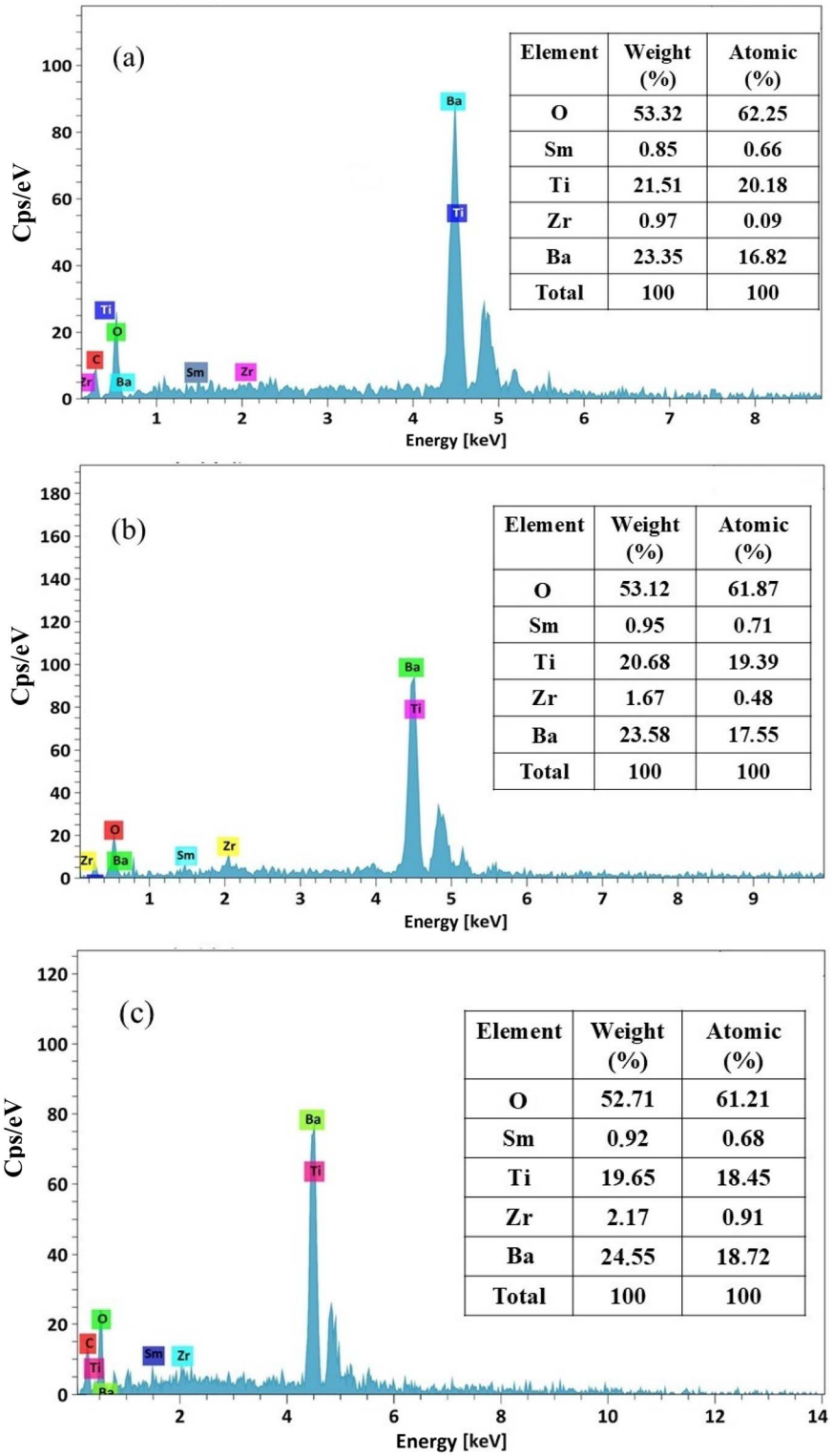

Fig. 8 Elemental composition (EDX spectra) for the ceramics (a) ZrSm0.01, (b) ZrSm0.05, and (c) ZrSm0.10. Inset: weight% and atomic% of chemical elements in the samples.

The distances between the atoms located in the A site (Ba/Sm), the B site (Ti/Zr), and the oxygens O1 and O2 are listed in Table 3. The analysis of these data shows that the displacement of (Ti/Zr) atoms within the B site along the *c*-axis decreases as the Zr concentration increases (see Fig. 6). This indicates a more pronounced distortion of the [Ti/ZrO_6] octahedra in the $Ba_{0.95}Sm_{0.034}Ti_{(1-x)}Zr_xO_3$ ceramic for SmZr0.10 compared to other compositions. The increase in this distortion in the Zr-rich compound could be associated with a reduction in tetragonality. This enhanced distortion is also a key factor in explaining the decrease in the Curie temperature (T_C), as will be detailed in the section dedicated to dielectric properties.

3.2. Density and microstructure

3.2.1. Relative density. The relative density (ρ_r) of the ZrSm0.01, ZrSm0.05, and ZrSm0.10 ceramics was determined using the Archimedes method. The values of relative density (ρ_r), measured density (ρ_m), and theoretical density (ρ_{th}) of the prepared ceramics are presented in Table 4. These results suggest that the densification of the samples increases proportionally with the Zr concentration.

3.2.2. Microstructure of ceramics. Fig. 7(a)–(c) show the SEM micrographs of the ZrSm0.01, ZrSm0.05, and ZrSm0.10 ceramics, while Fig. 7(d)–(f) present the corresponding grain size distributions. The Zr poor samples exhibit more visible pores, whose presence decreases as the Zr content increases. Both the grains and their boundaries are clearly distinguishable in all samples. The average grain size increases gradually with Zr concentration: 1.52 μm for ZrSm0.01, 1.974 μm for ZrSm0.05, and 2.184 μm for ZrSm0.10. This grain growth may be attributed to the higher concentration of oxygen vacancies generated with increasing Zr, which can enhance mass transport during sintering. Despite this increase, the grains remain significantly smaller than those reported for rare earth free BZT ceramics, such as $BaZr_{0.05}Ti_{0.95}O_3$ (~5 μm)[48] and $BaZr_{0.10}Ti_{0.90}O_3$ (~10 μm),[49] highlighting the grain growth inhibiting effect of Sm and Zr co-substitution.

The chemical composition of the ceramics was determined using EDX spectroscopy. The electron beam causes ionization of the atoms' inner shells, leading to the emission of characteristic signals that are analyzed to identify the elemental composition of the ceramic under study. The EDX spectra presented in Fig. 8(a)–(c) show peaks corresponding to the elements Ba, Ti, Zr, Sm, and O, confirming the successful incorporation of all targeted ions into the crystalline matrix. The presence of carbon in the apparent composition of the samples is related to the sample holder used during the EDX analysis. The elemental composition of the samples was also examined by EDX (see the inset of Fig. 8(a)–(c)). Theoretically, for pure $BaTiO_3$ ceramic, the atomic ratio Ba : Ti : O is close to 1 : 1 : 3.[50] In our ZrSm0.01, ZrSm0.05, and ZrSm0.10 samples,

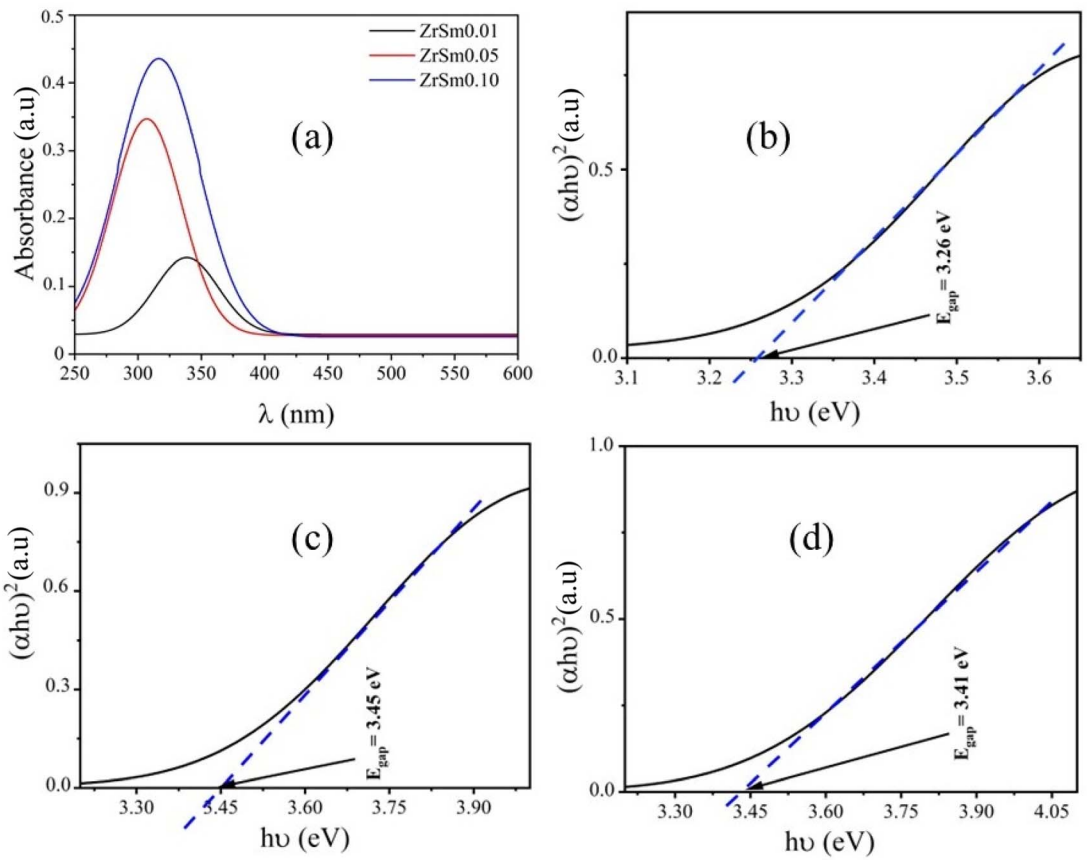

Fig. 9 (a) Absorbance spectra in the 250–600 nm range. (b–d) Plot of $(\alpha h\nu)^2$ as a function of photon energy $h\nu$ for the ZrSm0.01, ZrSm0.05, and ZrSm0.10 ceramics.

the measured atomic percentages are very close to the theoretical values expected from the synthesis. Overall, the EDX results confirm the successful substitution of Ti^{4+} by Zr^{4+} in the $Ba_{0.95}Sm_{0.034}Ti_{(1-x)}Zr_xO_3$ ceramics.

3.3. UV-VIS spectroscopic analysis

The UV-Vis absorption spectra of the prepared ZrSm0.01, ZrSm0.05, and ZrSm0.10 ceramics are shown in Fig. 9(a). Increasing the zirconium content causes a shift of the absorption peaks, initially located between 300 and 350 nm, toward shorter wavelengths. This absorption band is associated with electronic transitions between the conduction band, composed of Ti^{4+} ($3d^1$) and Zr^{4+} ($4d^1$) states, and the valence band, formed by O^{2-} (2p) states.[51]

The optical bandgap energy (E_{gap}) of the ZrSm0.01, ZrSm0.05, and ZrSm0.10 ceramics was determined using the Beer–Lambert law.[43,52–54]

$$(\alpha h\nu)^2 = C(h\nu - E_{gap}), \quad \alpha = \frac{\ln(T)}{t} \tag{1}$$

In this relation, E_{gap} represents the optical bandgap energy, $h\nu$ is the incident photon energy (with ν being the light frequency and h Planck's constant), C is an energy-independent constant, α is the optical absorption coefficient, T is the transmittance, and t is the thickness of the cylindrical disk. The curves representing $(\alpha h\nu)^2$ *versus* $(h\nu)$ are plotted in Fig. 9(b)–(d).

Table 5 presents the optical bandgap (E_{gap}) values of the materials prepared in this work, along with those of various compounds reported in the literature. These data enable a comparison of the effect of substituting titanium (Ti^{4+}) with zirconium (Zr^{4+}) on the bandgap energy. The samples with the

Table 5 Band-gap energy values of ZrSm0.01, ZrSm0.05, and ZrSm0.10 ceramics compared with those of materials reported in the literature

Compounds	E_{gap}	References
$BaTiO_3$	3.10–3.20	57
$BaTi_{0.95}Zr_{0.05}O_3$	3.15	35
$BaTi_{0.90}Zr_{0.10}O_3$	3.09	58
$Ba_{0.99}Sm_{0.0067}Ti_{0.95}Zr_{0.05}O_3$	3.07	35
$Ba_{0.98}Sm_{0.013}Ti_{0.95}Zr_{0.05}O_3$	3.05	35
$Ba_{0.97}Sm_{0.02}Ti_{0.95}Zr_{0.05}O_3$	3.02	35
$Ba_{0.95}Sm_{0.034}Ti_{0.99}Zr_{0.01}O_3$	3.26	Present work
$Ba_{0.95}Sm_{0.034}Ti_{0.95}Zr_{0.05}O_3$	3.45	Present work
$Ba_{0.95}Sm_{0.034}Ti_{0.90}Zr_{0.10}O_3$	3.41	Present work

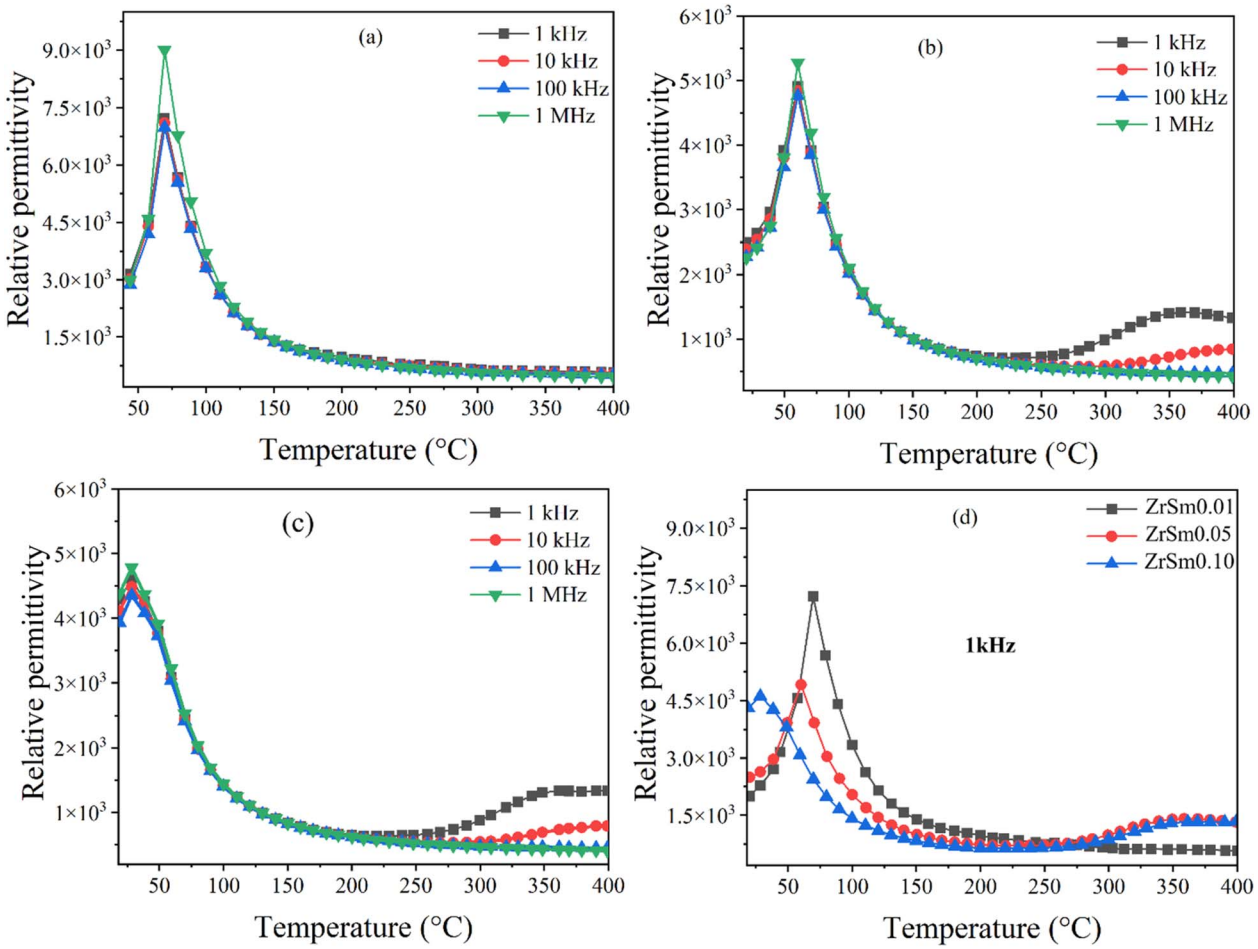

Fig. 10 Evolution of the relative permittivity for (a) ZrSm0.01, (b) ZrSm0.05, and (c) ZrSm0.10. (d) Comparison of the relative permittivity at 1 kHz for all prepared ceramics.

composition $Ba_{0.95}Sm_{0.034}Ti_{(1-x)}O_3$ ($x \leq 0.10$), synthesized in the present work, exhibit optical bandgap (E_{gap}) values ranging from 3.26 eV to 3.45 eV. These values are higher than those reported for compounds such as $BaTiO_3$, $BaTi_{0.95}Zr_{0.05}O_3$ and $BaTi_{0.90}Zr_{0.10}O_3$, whose E_{gap} values range between 3.09 eV and 3.20 eV. These results indicate that the moderate introduction of Zr^{4+} into the perovskite structure of $BaTi_{(1-x)}O_3$ ($x \leq 0.10$) leads to a slight decrease in the bandgap energy. However, the co-substitution of Sm^{3+} at the Ba-site and Zr^{4+} at the Ti-site in compounds of the type $Ba_{1-x}Sm_{2x/3}Ti_{0.95}Zr_{0.05}O_3$ ($x \leq 0.03$), leads to a gradual decrease in the bandgap energy. In general, the variation in bandgap energy is strongly dependent on the chemical composition of the materials. However, other factors can also influence this energy, including structural distortions and the formation of intermediate energy levels within the bandgap, which are associated with the introduction of trivalent ions.[40,55] The optical band gap values obtained in this study (3.26 eV, 3.45 eV, and 3.41 eV) show that the $Ba_{0.95}Sm_{0.034}Ti_{(1-x)}Zr_xO_3$ ceramics exhibit an optical gap compatible with all-dielectric photonic applications. Considering their ferroelectric nature and high-refractive-index characteristics, these materials could be integrated into metasurface or photonic crystal architectures to explore the generation of localized optical modes and the enhancement of emission or optical coupling. These perspectives therefore open the way for the potential use of the studied compositions in advanced optical devices and highly sensitive detection platforms.[56]

3.4. Investigation of the dielectric properties

3.4.1. Temperature dependence of the relative permittivity. The temperature-dependent behavior of the relative permittivity for the ZrSm0.01, ZrSm0.05, and ZrSm0.10 ceramics is presented in Fig. 10(a)–(c). All three samples display a pronounced dielectric peak, which marks the transition from the tetragonal ferroelectric phase to the cubic paraelectric phase.[59] It is also noteworthy that the transition temperature, or Curie temperature (T_C), remains constant regardless of frequency, confirming the absence of relaxor behavior in the prepared ceramics. This suggests that a low amount of Zr^{4+} substitution ($0.01 \leq x \leq 0.10$) does not induce a significant relaxor state in our samples, likely due to the similar ionic radii and the same valence between Zr^{4+} and Ti^{4+} ions.[39] T_C for the ZrSm0.01, ZrSm0.05, and ZrSm0.10 compounds are 69 °C, 57 °C, and 28 °C, respectively. On the other hand, the maximum relative permittivity values (ε'_{max}) at T_C for the ceramics with compositions ZrSm0.01, ZrSm0.05, and ZrSm0.10 are 7228, 4903, and 4611, respectively, at 1 kHz.

These materials exhibit a clear dependence between the relative permittivity, the T_C, and the increasing Zr content. The introduction of Zr reduces the maximum relative permittivity (ε'_{max}), broadens the dielectric peak, and shifts the T_C to lower values, likely due to lattice distortion induced by the substitution of Ti^{4+} with Zr^{4+}.[60] Fig. 10(d) shows the relative permittivity at 1 kHz for all synthesized ceramics as a function of temperature. The modification of the lattice parameter induces a shift

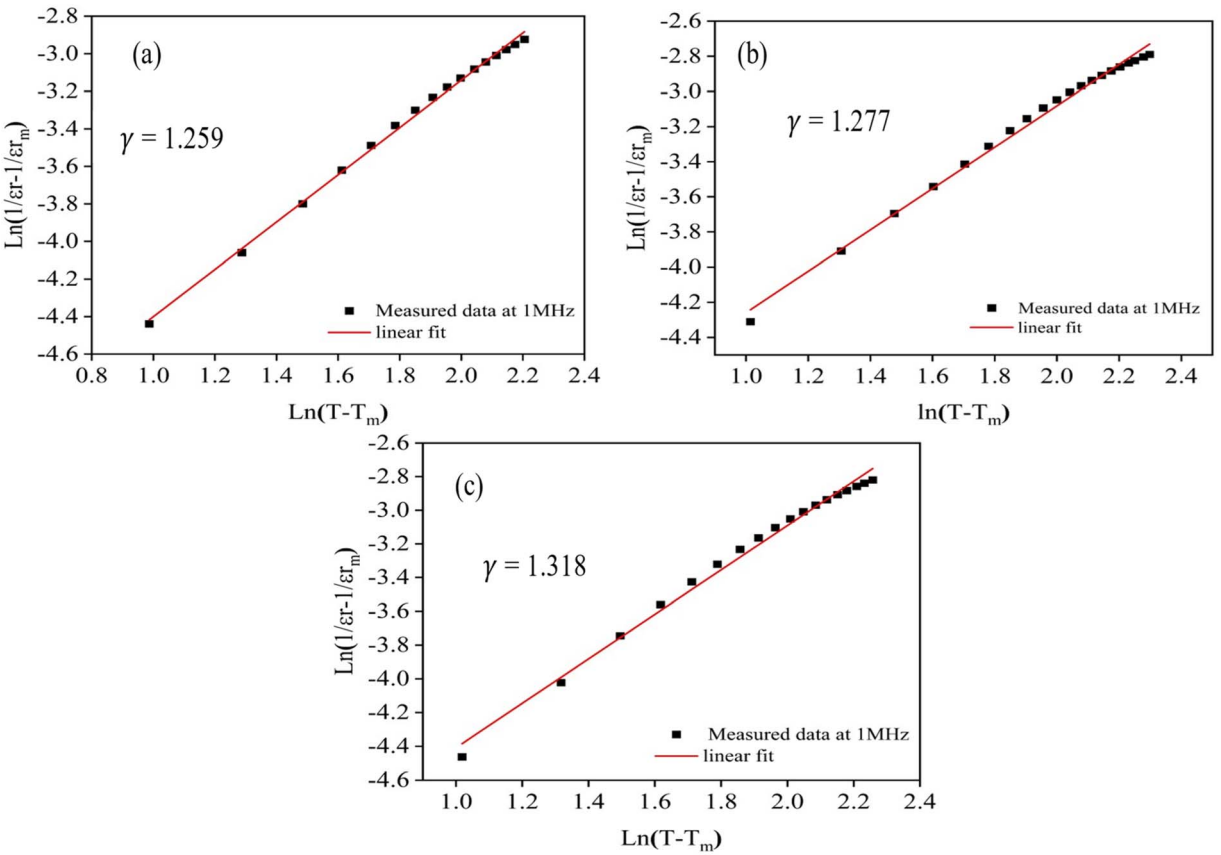

Fig. 11 Curves of $\ln(1/\varepsilon' - 1/\varepsilon'_{max})$ as a function of $\ln(T - T_m)$ at 1 MHz for the samples (a) ZrSm0.01, (b) ZrSm0.05, and (c) ZrSm0.10.

of Ti^{4+}/Zr^{4+} ions along the *c*-axis, thereby increasing the distortion of the $[Ti^{4+}/Zr^{4+}O_6]$ octahedra. This distortion weakens the coupling between the $[Ti^{4+}/Zr^{4+}O_6]$ octahedral groups, leading to a reduction in the T_C and a decrease in the dielectric performance of the studied ceramics.

To analyze dielectric dispersion and the diffuse nature of phase transitions in ferroelectric materials, Uchino and Nomura introduced an empirical formula commonly referred to as the modified Curie–Weiss law.[61,62] This expression is given as follows:

$$1/\varepsilon' - 1/\varepsilon'_{max} = \frac{(T - T')^{\gamma}}{A'} \quad (2)$$

ε'_{max} represents the maximum relative permittivity at the temperature T', A' is the Curie–Weiss constant, the diffusivity coefficient γ equals 1 for a conventional ferroelectric and reaches 2 for a relaxor ferroelectric. When γ takes a value between 1 and 2, it signifies a partially diffuse phase transition.[23,63,64] Fig. 11(a)–(c) shows the variation of $\ln(1/\varepsilon' - 1/\varepsilon'_{max})$ as a function of $\ln(T - T_m)$ at 1 MHz for all the prepared ceramics in the temperature range $T > T_C$. The red line represents the fit to the modified Curie–Weiss law, while the scattered points correspond to the experimental data. A linear relationship is observed for all compositions, with γ values systematically calculated from the slope of each curve. The calculated γ values for ZrSm0.01, ZrSm0.05, and ZrSm0.10 ceramics are 1.259, 1.277, and 1.318, respectively. These γ values, which lie between 1 and 2, clearly indicate that these ceramics exhibit an incomplete diffuse phase transition. Furthermore, the gradual increase in γ with increasing Zr content suggests a continuous improvement in the relaxation behavior of the ceramics.[60]

3.4.2. Frequency dependence of relative permittivity. To better understand the dielectric relaxation behaviors in these ceramics and their evolution with increasing Zr content, a study of the relative permittivity variation as a function of frequency was conducted. The variation of $\ln(\varepsilon')$ with frequency for the ceramics is shown in Fig. 12(a)–(c). It is observed that the relative permittivity of our samples is high at low frequency and decreases as the frequency increases. At low frequencies, a material can exhibit various polarization mechanisms, such as interfacial, space charge, dipolar, ionic, and electronic polarization.[65] Dipolar and interfacial polarization mechanisms are especially sensitive to the frequency of the applied electric field.

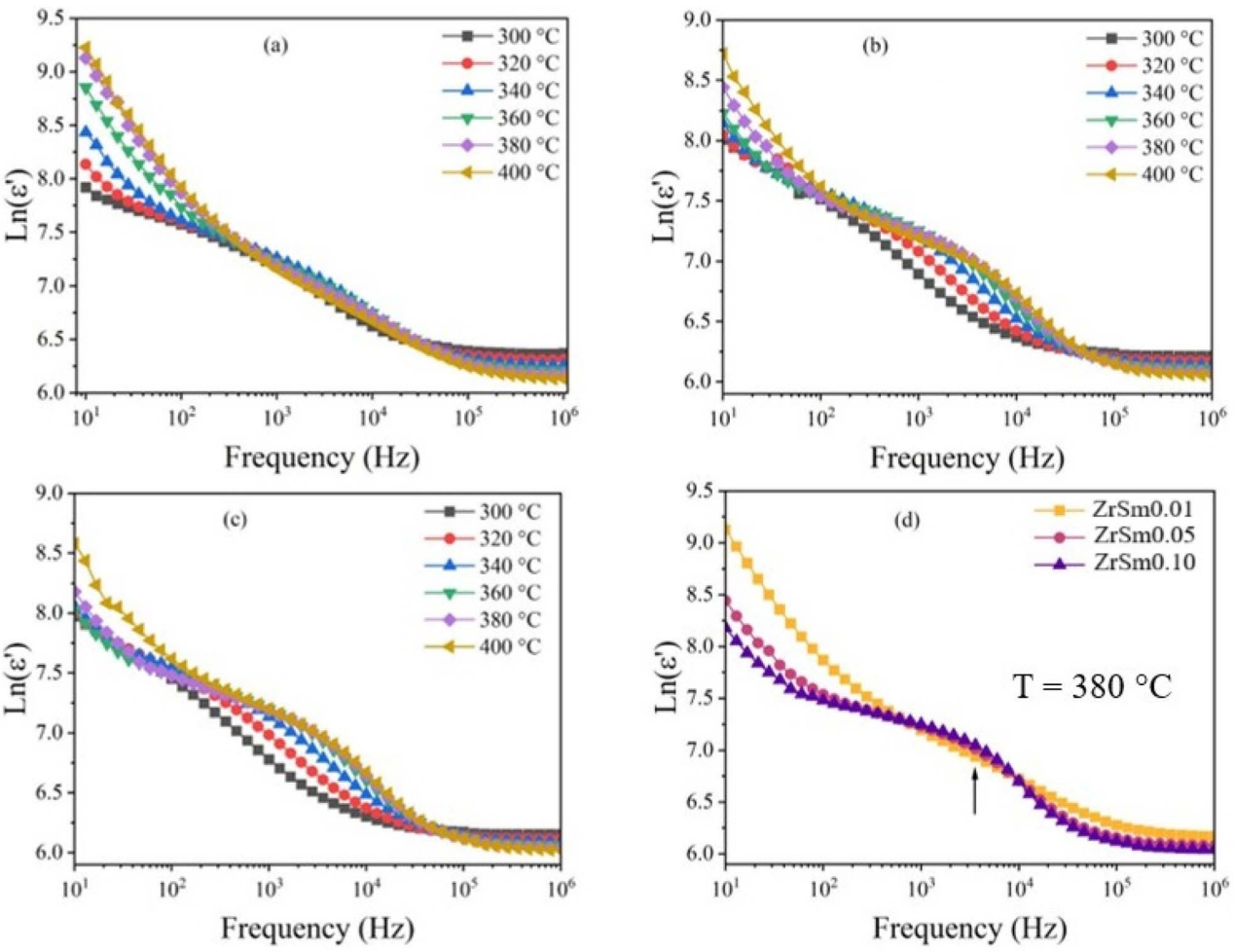

Fig. 12 Evolution of $\ln(\varepsilon')$ as a function of frequency at various temperatures for the samples: (a) ZrSm0.01, (b) ZrSm0.05, and (c) ZrSm0.10. (d) shows the comparison of $\ln(\varepsilon')$ *versus* frequency at $T = 380$ °C.

The reduction in permittivity observed with increasing frequency arises because the polarized dipoles and/or charge carriers within the material are unable to keep pace with the changing direction of the electric field. This behavior also manifests in how permittivity varies according to the material's composition.

Dielectric relaxation in these compositions occurs between frequencies of 10^3 Hz and 10^4 Hz. A shift towards higher frequencies is observed as the temperature increases. The dependence of relative permittivity on the composition of the prepared ceramics is shown in Fig. 12(d). It is clear that the dielectric permittivity decreases with increasing Zr content. Furthermore, the dielectric relaxation behavior becomes more pronounced as the Zr concentration increases. The enhancement of the relaxation behavior in dielectric ceramics is a crucial factor for optimizing their energy storage properties, as demonstrated in several studies.[42,60,66]

3.4.3. Dielectric loss. Fig. 13(a)–(c) illustrates the change in dielectric loss (tan δ) with temperature at various frequencies for the ceramics ZrSm0.01, ZrSm0.05, and ZrSm0.10. Two distinct regions are observed, ranging from ambient temperature to 400 °C. The first region, from room temperature to 250 °C, exhibits significantly low values of tan(δ). The low tan(δ) values observed in this region result from the restricted electron diffusion at the grain boundaries.[67] These grain boundaries, where the crystalline structures of adjacent grains meet, are typically sites of energy dissipation linked to electron mobility.[38] In the ceramics ZrSm0.01, ZrSm0.05, and ZrSm0.10, the limited electron diffusion at the grain boundaries reduces energy loss, resulting in lower tan(δ) values. In the high-temperature range (250 °C to 400 °C), a significant increase in tan(δ) is observed. This behavior is mainly attributed to space charge polarization, which becomes prominent at elevated temperatures. Under these conditions, electrical conductivity dominates the dielectric response, while the influence of ferro-elastic domain walls remains minimal, leading to a rapid rise in tan(δ).[68] The defining feature of ferroelectric materials is their ability to exhibit spontaneous polarization, which can be reversed under the influence of an external electric field. This behavior arises from the unit cell symmetry, which allows at least two equivalent directions for polarization. The material is divided into regions, called domains, where the polarization remains uniform, and these are separated by natural interfaces known as domain walls.[69] The minimal influence of ferroelectric domain walls indicates that, at high temperatures, their contribution to tan(δ) is reduced. As a result, the value of tan(δ) increases with rising temperature.

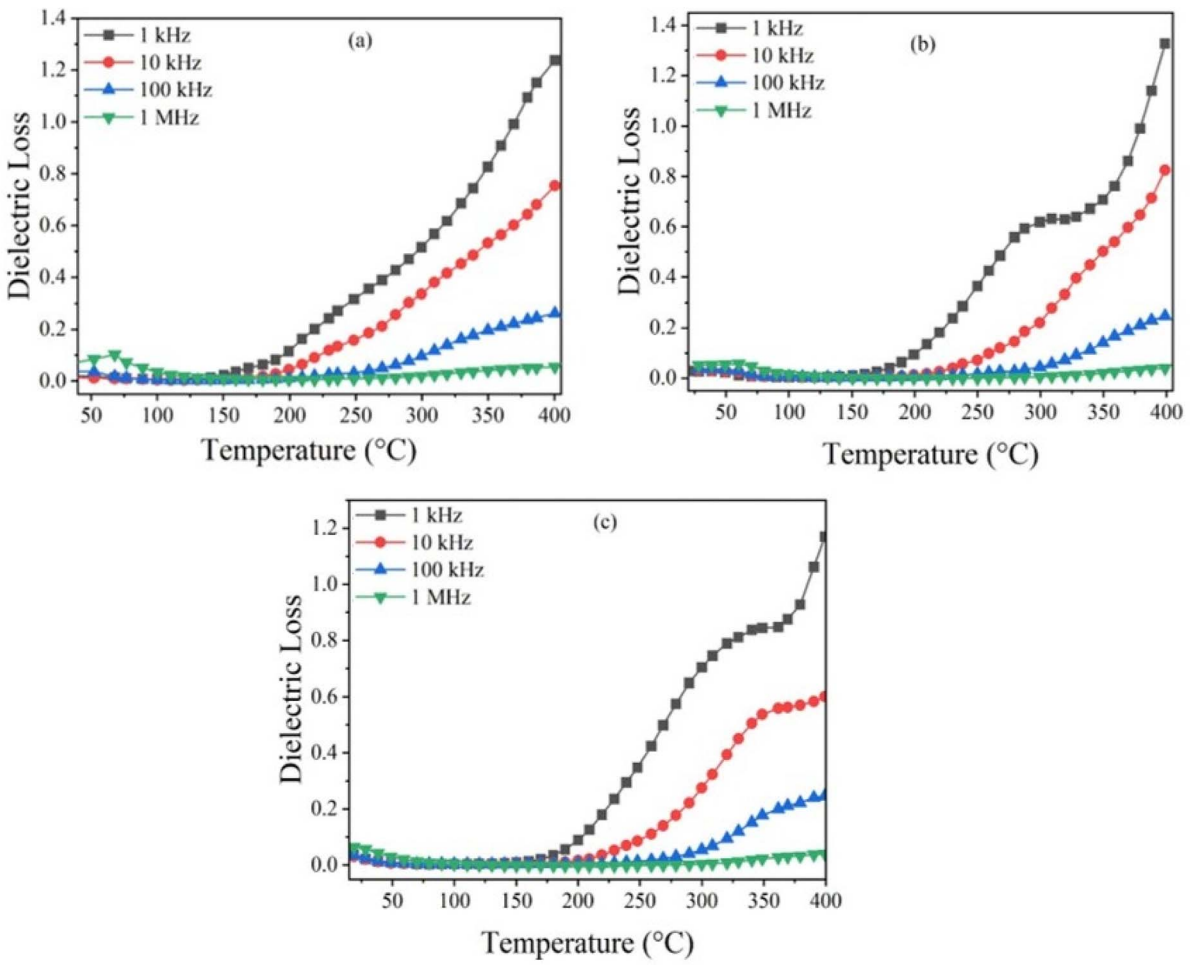

Fig. 13 Dielectric loss evolution for: (a) ZrSm0.01, (b) ZrSm0.05, and (c) ZrSm0.10.

A broad peak (anomaly) is found in the loss tangent graphs at high temperatures. This peak becomes more pronounced with increasing Zr concentration. The behavior observed in high-temperature regions is related to the dielectric relaxation process. This thermally activated relaxation mechanism is attributed to dipolar effects associated with the movement of charge carriers (electrons) within the grains.[70]

3.5. Study on the electrical response

In this section, we conduct a detailed analysis of the Nyquist diagrams and the electric modulus of the prepared ceramics. This study aims to deepen the understanding of charge transport mechanisms, dielectric relaxation processes, and the contributions of various polarization phenomena. We also highlight the correlations between the microstructural properties and the electrical responses of the studied materials.

3.5.1. Nyquist. The Nyquist diagrams presented in Fig. 14(a)–(c) for the ceramics ZrSm0.01, ZrSm0.05, and ZrSm0.10 at different temperatures show arcs with their center positioned above the real axis (x). As the temperature increases, these arcs become more complete within the measured frequency range (10 Hz to 1 MHz). This results in a decrease in the arc diameter, indicating a reduction in the overall resistance of the material. The intersection of the arc with the real axis Z' in the complex impedance diagram provides an estimate of the material's total resistance.[71,72] Additionally, the appearance of off-center curves confirms a non-Debye type relaxation in the samples.[73] It is observed in the Nyquist diagram that there are two depressed

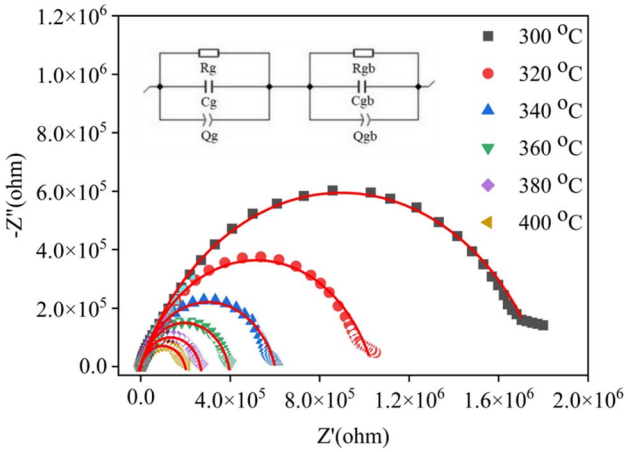

Fig. 15 Nyquist diagram fitted for ZrSm0.10.

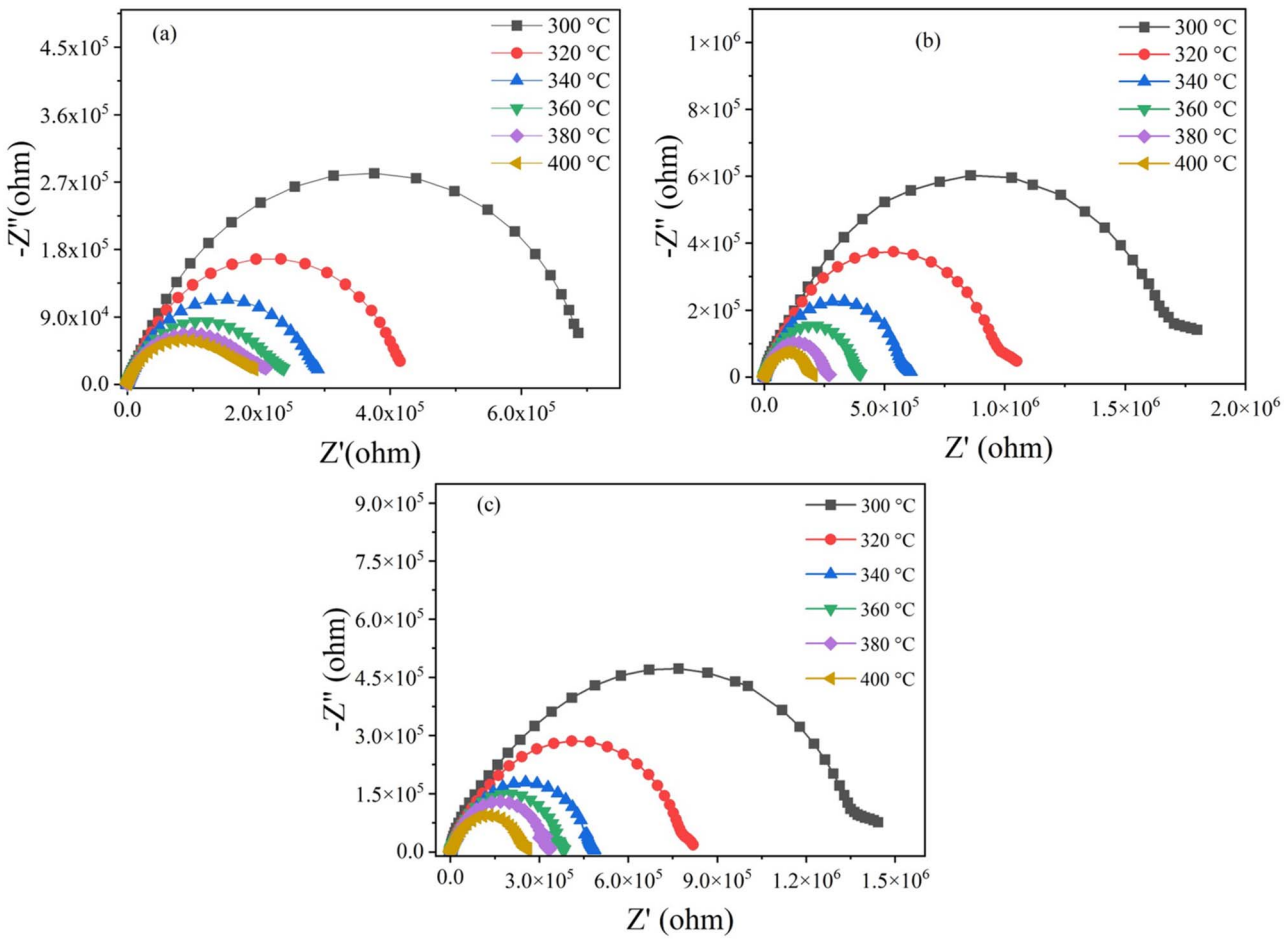

Fig. 14 Nyquist diagrams of the ceramics (a) ZrSm0.01, (b) ZrSm0.05, and (c) ZrSm0.10.

Table 6 The parameters obtained from the fitting of the experimental data of the Nyquist diagram for the ceramics ZrSm0.01, ZrSm0.05, and ZrSm0.10

	T (°C)	R_g (kΩ)	Q_g (F $s^{(\alpha-1)}$)	α_g	R_{gb} (kΩ)	Q_{gb} (F $s^{(\alpha-1)}$)	α_{gb}
ZrSm0.01	300	720.074	6.64×10^{-9}	0.7243	138.47	01.05×10^{-9}	0.9774
	320	422.832	6.31×10^{-9}	0.7525	82.99	02.68×10^{-9}	0.300
	340	290.585	7.42×10^{-9}	0.7404	55.80	08.83×10^{-9}	0.1617
	360	238.872	15.49×10^{-9}	0.6582	31.75	21.22×10^{-9}	0.1820
	380	216.350	35.39×10^{-9}	0.5696	20.67	48.97×10^{-9}	0.9999
	400	201.221	54.02×10^{-9}	0.5250	17.64	16.82×10^{-9}	0.9964
ZrSm0.05	300	1397	12.77×10^{-9}	0.5556	79.183	3.052×10^{-9}	0.6593
	320	797.678	9.545×10^{-9}	0.6182	49.351	14.14×10^{-9}	0.4466
	340	472.167	7.863×10^{-9}	0.6556	29.831	67.13×10^{-10}	0.2492
	360	368.014	4.978×10^{-9}	0.7020	17.605	48.98×10^{-10}	0.2164
	380	320.112	5.298×10^{-9}	0.6908	12.082	58.64×10^{-10}	0.8656
	400	246.647	10.17×10^{-9}	0.6346	9.879	45.45×10^{-10}	0.9894
ZrSm0.10	300	1779	10.36×10^{-9}	0.5975	52.308	06.78×10^{-9}	0.5998
	320	1020	8.879×10^{-9}	0.6329	33.876	12.315×10^{-9}	0.9594
	340	579.937	9.003×10^{-9}	0.6158	16.176	14.62×10^{-9}	0.5673
	360	381.627	6.112×10^{-9}	0.6871	12.598	21.09×10^{-9}	0.2962
	380	254.366	3.805×10^{-9}	0.7676	10.322	25.44×10^{-9}	0.9953
	400	191.644	17.25×10^{-9}	0.5683	8.042	27.64×10^{-9}	0.9996

semicircles, indicating two distinct contributions. The first, at low frequencies, shows a contribution from the grain boundaries, while the second, at high frequencies, is attributed to the grains.[74]

The fitting of the experimental data from the Nyquist diagrams using the appropriate equivalent electrical circuit with the MT-Lab software showed that the results are in good agreement with an equivalent electrical circuit consisting of two series-connected cells, corresponding to the grains and the grain boundary effects, respectively. Fig. 15 shows the fitting of the Nyquist diagram using the appropriate equivalent electrical model for ZrSm0.10. The various adjusted parameters are presented in Table 6.

The results presented in Table 6 show an increase in the values of R_g and a decrease in the values of R_{gb} with the increase in the amount of Zr. Additionally, it is observed that these values (R_g and R_{gb}) decrease with the rise in temperature for all ceramics, suggesting the thermal activation of conduction mechanisms in these materials. The values of R_g and R_{gb} were evaluated using the Arrhenius law to determine the activation energy associated with each.[75,76]

$$R = R_0 \exp(-E_a/k_B T) \quad (3)$$

where E_a represents the activation energy for conduction, k_B the Boltzmann constant, R_0 the pre-exponential factor, and T the temperature (in K). The values of E_g (activation energy of the grains) and E_{gb} (activation energy of the grain boundaries), obtained from the linear fit according to the Arrhenius law equation, are shown in Fig. 16(a) and (b). The corresponding results are detailed in Table 7.

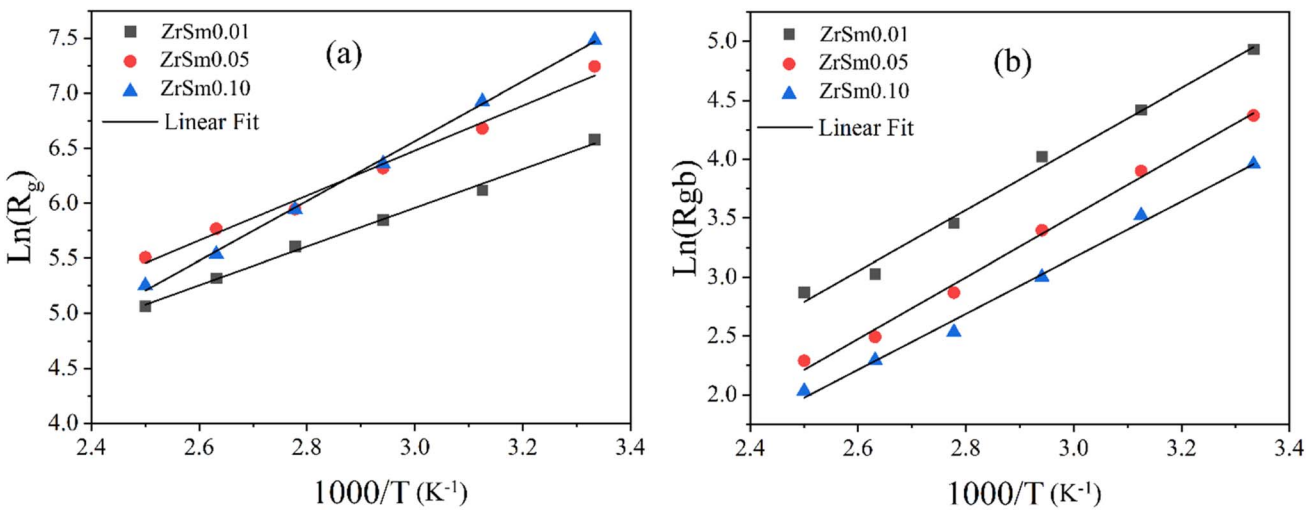

Fig. 16 Arrhenius plots of the data obtained for the ZrSm0.01, ZrSm0.05, and ZrSm0.10 ceramics: (a) for the grains, and (b) for the grain boundaries.

Table 7 Ea values related to R_g and R_{gb} for ZrSm0.01, ZrSm0.05, and ZrSm0.10 ceramics

Compositions	E_a/eV (grain boundaries)	E_a/eV (grains)
ZrSm0.01	0.631	0.573
ZrSm0.05	0.612	0.530
ZrSm0.10	0.484	0.405

The activation energies of the grains range from 0.484 to 0.631 eV, while the activation energies of the grain boundaries range from 0.405 to 0.573 eV, for temperatures between 300 °C and 400 °C. It is clear that as the Zr content increases, the activation energy decreases.

The activation energy (E_a) represents the total energy required both to generate charge carriers and to enable their long-range migration, also known as the free-jump energy.[77,78] In ferroelectric ceramics, this energy associated with small polarons typically ranges from 0.2 to 1.5 eV.[79] It is influenced by the motion of domain walls, which depends on potential barriers at the grain boundaries that become more pronounced at elevated temperatures. These barriers are related to lattice distortions and grain size, both of which can limit the mobility of small polarons.[80] The high activation energy observed for the low-zirconium-content compound is attributed to the low densification of these samples, as the presence of pores increases the energy required for charge carriers to perform their jumps.

3.5.2. Impedance modulus. Fig. 17(a)–(c) show the imaginary part of the electric modulus (M'') as a function of frequency, measured at different temperatures for the ZrSm0.01, ZrSm0.05, and ZrSm0.10 ceramics. The variation of M'' with frequency is characterized by the presence of two peaks. An asymmetric peak appears at low frequency, while another peak is observed at high frequency, which are attributed to the relaxation processes of the grains and grain boundaries, respectively.

It is observed that, with increasing temperature, the relaxation peaks shift to higher frequencies. The presence of two peaks at distinct frequencies can be attributed to two different relaxation processes. At low frequency, the observed peak is associated with the long-range mobility of ions, which move from one site to another through hopping.[81,82] At high frequency, however, the charge carriers are primarily confined within their potential wells, moving over short distances and undergoing only localized motions within these wells.[83–88]

The asymmetry of the relaxation peaks (M''_{max}) reveals the presence of a stretching coefficient (β). This parameter allows characterization of the relaxation process type, whether Debye or

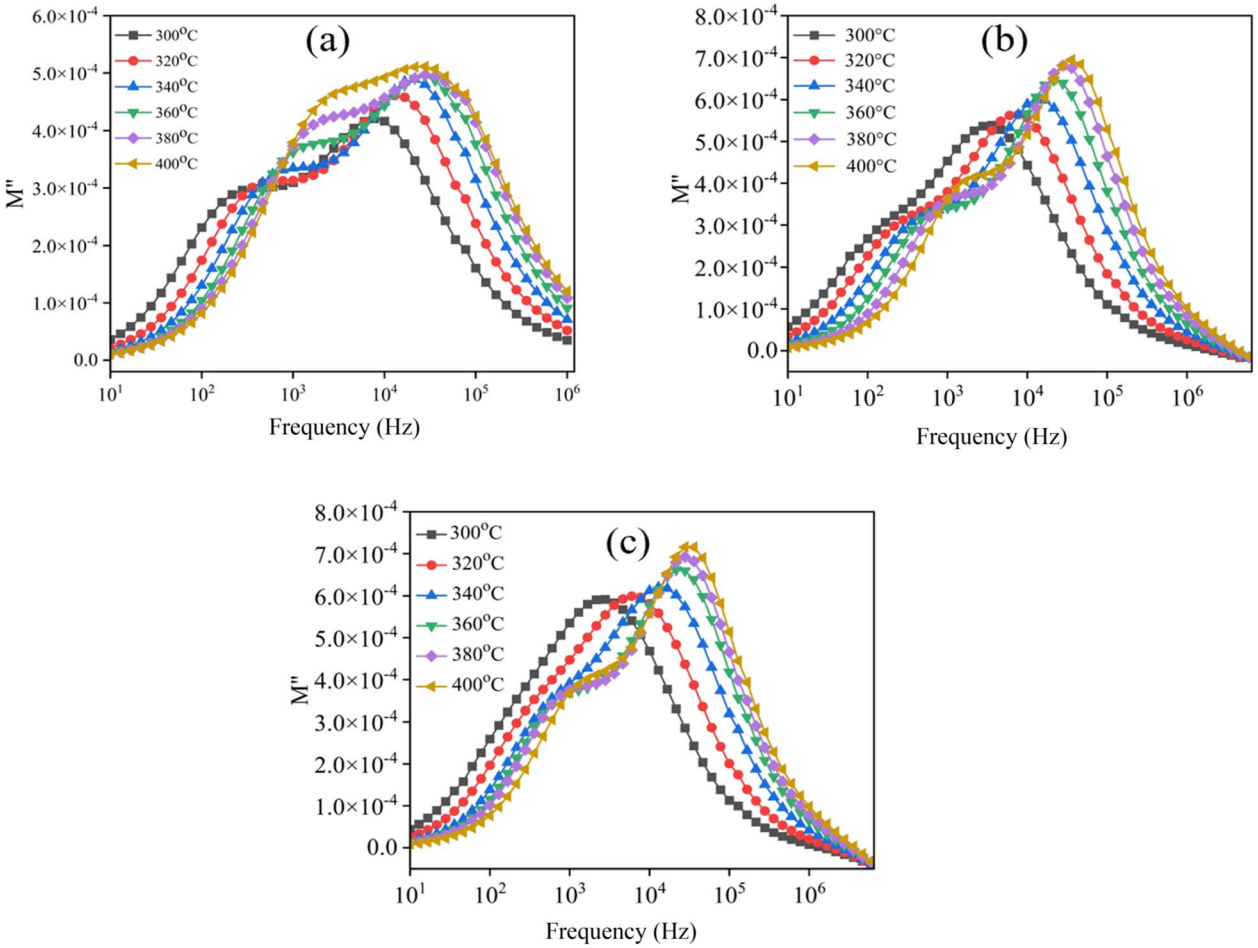

Fig. 17 M'' as a function of frequency at various temperatures for (a) ZrSm0.01, (b) ZrSm0.05, and (c) ZrSm0.10.

non-Debye, and helps determine if the relaxation originates from the grains or the grain boundaries.[84] To verify this, the stretching coefficient (β) was determined by fitting the imaginary part of the electric modulus (M'') using the Kohlrausch–Williams–Watts (KWW) function for a single M'' response, or the modified KWW function for a double response, according to Bergman's approach:[89]

$$M'' = \frac{M''^{g}_{max}}{(1-\beta_g) + \frac{\beta_g}{1+\beta_g}\left[\beta_g\left(\frac{f^{g}_{max}}{f}\right) + \left(\frac{f}{f^{g}_{max}}\right)^{\beta_g}\right]} \quad (4)$$

$$M'' = \frac{M''^{g}_{max}}{(1-\beta_g) + \frac{\beta_g}{1+\beta_g}\left[\beta_g\left(\frac{f^{g}_{max}}{f}\right) + \left(\frac{f}{f^{g}_{max}}\right)^{\beta_g}\right]} + \frac{M''^{gb}_{max}}{(1-\beta_{gb}) + \frac{\beta_{gb}}{1+\beta_{gb}}\left[\beta_{gb}\left(\frac{f^{gb}_{max}}{f}\right) + \left(\frac{f}{f^{gb}_{max}}\right)^{\beta_{gb}}\right]} \quad (5)$$

M''^{gb}_{max} represents the maximum value of M'' in the low-frequency region, while M''^{g}_{max} corresponds to the maximum value in the high-frequency region. f^{gb}_{max} is the peak frequency associated with the grain boundary anomaly, and f^{g}_{max} corresponds to the grain-related anomaly. For ideal Debye-type relaxation, $\beta = 1$, whereas for non-Debye relaxation, β ranges between 0 and 1 ($0 < \beta < 1$). Fig. 18(a) and (b) shows the variation of β as a function of temperature, taking into account the contributions from both grains and grain boundaries. The β values, lying between 0 and 1, indicate a non-Debye behavior for all the ceramics studied. The relaxation times τ_g and τ_{gb} were analyzed using the Arrhenius law to determine the activation energies associated with the contributions of grains and grain boundaries.[14]

$$\tau^{M''} = \tau_0 \exp(E_a/k_B T) \quad (6)$$

where E_a represents the activation energy, k_B the Boltzmann constant, τ_0 the pre-exponential factor, and T the temperature (in K). Fig. 18(c) shows the Arrhenius plot for the grain boundary response, while Fig. 18(d) illustrates the plot for the

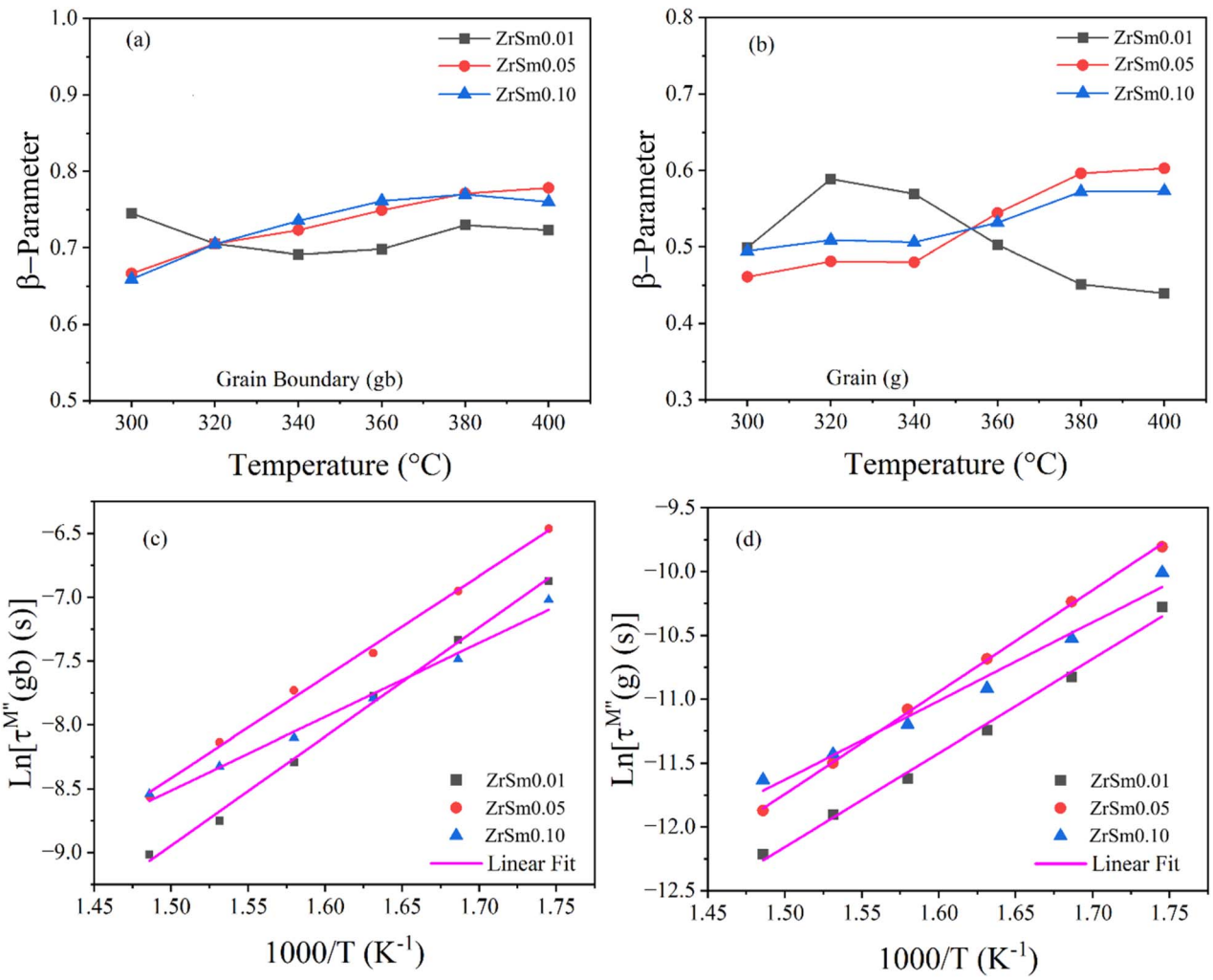

Fig. 18 The evolution of the β parameter with temperature is shown for all ceramics in (a) grain boundaries and (b) grains. The corresponding Arrhenius plots of $\ln(\tau^{M''})$ *versus* $1000/T$ are presented in (c) for grain boundaries and (d) for grains.

Table 8 Activation energy values associated with $\tau^{M''}$ for the ZrSm0.01, ZrSm0.05, and ZrSm0.10 ceramics

Compositions	E_a/eV (grains)	E_a/eV (grain boundary)
ZrSm0.01	0.635	0.736
ZrSm0.05	0.609	0.689
ZrSm0.10	0.498	0.498

grain response. The activation energy associated with each response was determined from the slope of the linear fits on these graphs. The calculated activation energy values, $E_{a(gb)}$ and $E_{a(g)}$, for our materials are presented in Table 8.

Comparison of the activation energy values suggests that more energy is required for charge carriers to jump across the grain boundaries than within the grains. This can be explained by the fact that the movement of charge carriers inside the grains is confined to the oxygen octahedra of the unit cell, whereas at the grain boundaries, the diffusion or hopping of charge carriers requires more energy.[88] It is important to note that a slight discrepancy was observed between the activation energies calculated from the Nyquist data (see Table 7) and those obtained from M'' data (see Table 8). This difference can be explained by the fact that Z'' primarily reflects the overall macroscopic behavior, while M'' is governed by the microscopic behavior of domains or grains within the sample.

4. Conclusion

The different compositions $Ba_{0.95}Sm_{0.034}Ti_{(1-x)}Zr_xO_3$ with $x =$ 0.01, 0.05, and 0.10 were synthesized *via* the solid-state reaction method at 1200 °C for 6 hours in air. The ceramics were then sintered at 1300 °C for 6 hours. The structural study by X-ray powder diffraction for all compounds reveals crystallization in a tetragonal structure with the space group *P*4*mm*. Increasing the zirconium content substituting titanium leads to an increase in the unit cell volume and a significant distortion of the [Ti/ZrO_6] octahedra. All samples exhibit a dense microstructure with pores that decrease as the Zr content increases. Additionally, the average grain size also increases with the rising Zr content. The bandgap energy (E_{gap}) of the ZrSm0.01, ZrSm0.05, and ZrSm0.10 ceramics ranges between 3.20 and 3.45 eV. The study of the dielectric properties of ZrSm0.01, ZrSm0.05 and ZrSm0.10 ceramics, as a function of temperature and frequency, revealed the presence of a dielectric peak associated with the transition from the ferroelectric to the paraelectric phase, corresponding to the Curie temperature. These results are consistent with the X-ray diffraction findings. A reduction in the Curie temperature was observed as the zirconium content increased. The evolution of the dielectric permittivity as a function of frequency at different temperatures shows that the relaxation behavior is enhanced with increasing Zr content. The electrical properties of the prepared ceramics are influenced by two distinct responses, one corresponding to the grain effect at low frequencies and the other related to the grain boundary response. Increasing the Zr content in the prepared compounds results in higher electrical resistance. The study of the complex modulus reveals non-Debye behavior for all analyzed ceramics. The activation energy determined from this modulus shows that charge carrier hopping mainly occurs across the grain boundaries rather than within the grains. The activation energy is higher at the grain boundaries than within the grains, reflecting the greater energy required for charge carriers to hop across boundaries. Overall, the activation energy decreases with increasing Zr content due to improved densification and reduced energy barriers.

Author contributions

El Hassan Yahakoub: conceptualization, investigation, writing – original draft. Khalid Lemrini: formal analysis, methodology, writing. Talal Moudrikah: investigation, software, methodology. El Houcine Lahrar: investigation, methodology. Slimane Raissi: resources, review & editing. Amine Bendahhou: methodology, formal analysis. Ilyas Jalafi: software, resources, review & editing. Fatima Chaou: methodology, writing. Soufian El Barkany: formal analysis, data curation, resources. Mohamed Abou-Salama: supervision and validation.

Conflicts of interest

The authors declare that they have no known competing financial interests or personal relationships that could have appeared to influence the work reported in this paper.

Data availability

Data will be made available on request.

Acknowledgements

This research did not receive any specific grant from funding agencies in the public, commercial, or not-for-profit sectors. The authors would like to express their sincere gratitude to the Laboratory of Molecular Chemistry, Materials, and Environment (LCM2E) at the Multidisciplinary Faculty of Nador, University Mohammed Premier, for its valuable technical assistance and support during the spectral analysis work. They also thank Mohammed Premier University of Oujda for its ongoing commitment to fostering high-level research and supporting the development of internationally oriented scientific projects. Their deepest appreciation goes to Professor Abdelmonaem Talhaoui, Head of the Chemistry Department in Oujda, for providing essential resources and unwavering support, which played a key role in the successful completion of this study.

References

1 N. Kumar, B. Narayan, A. K. Singh and S. Kumar, *Mater. Chem. Phys.*, 2020, **252**, 123313.
2 K. Shan, Z.-Z. Yi, X.-T. Yin, D. Dastan, F. Altaf, H. Garmestani and F. M. Alamgir, *Surf. Interfaces*, 2020, **21**, 100762.

3 F. El Bachraoui, Z. Chchiyai, Y. Tamraoui, H. El Moussaoui, J. Alami and B. Manoun, *J. Rare Earths*, 2022, **40**, 652–659.
4 K. Shan, Z.-Z. Yi, X.-T. Yin, L. Cui, D. Dastan, H. Garmestani and F. M. Alamgir, *J. Alloys Compd.*, 2021, **855**, 157465.
5 H. Tang, Y. Lin and H. A. Sodano, *Adv. Energy Mater.*, 2013, **3**, 451–456.
6 F. Chaou, I. Jalafi, F. Arhmir, K. Chourti, E. Hassan Yahakoub, A. Bendahhou, S. E. Barkany and M. Abou-Salama, *Mater. Chem. Phys.*, 2025, **339**, 130766.
7 F. Li, J. Zhai, B. Shen and H. Zeng, *J. Adv. Dielectr.*, 2018, **08**, 1830005.
8 U. Weber, G. Greuel, U. Boettger, S. Weber, D. Hennings and R. Waser, *J. Am. Ceram. Soc.*, 2001, **84**, 759–766.
9 C. Kajtoch, *J. Mater. Sci.*, 2011, **46**, 1469–1473.
10 L. Xu and Y. Xu, *J. Mater. Sci.: Mater. Electron.*, 2020, **31**, 5492–5498.
11 M. Reda, S. I. El-Dek and M. M. Arman, *J. Mater. Sci.: Mater. Electron.*, 2022, **33**, 16753–16776.
12 T. Maiti, R. Guo and A. Bhalla, *J. Am. Ceram. Soc.*, 2008, **91**, 1769–1780.
13 L. Jin, J. Qiao, L. Wang, L. Hou, R. Jing, J. Pang, L. Zhang, X. Lu, X. Wei, G. Liu and Y. Yan, *J. Alloys Compd.*, 2019, **784**, 931–938.
14 E. H. Yahakoub, A. Bendahhou, K. Chourti, F. Chaou, I. Jalafi, S. El Barkany, Z. Bahari and M. Abou-salama, *RSC Adv.*, 2022, **12**, 33124–33141.
15 S. Maity, A. Sasmal and S. Sen, *J. Alloys Compd.*, 2021, **884**, 161072.
16 I. Coondoo, N. Panwar, D. Alikin, I. Bdikin, S. S. Islam, A. Turygin, V. Y. Shur and A. L. Kholkin, *Acta Mater.*, 2018, **155**, 331–342.
17 X. Yan, M. Zheng, X. Gao, M. Zhu and Y. Hou, *J. Mater. Chem. C*, 2020, **8**, 13530–13556.
18 S. Smii, Y. Moualhi, F. Bahri and H. Rahmouni, *Phys. B*, 2023, **662**, 414966.
19 Y. Li, H. Cheng, H. Xu, Y. Zhang, P. Yan, T. Huang, C. Wang, Z. Hu and J. Ouyang, *Ceram. Int.*, 2016, **42**, 10191–10196.
20 M. Maraj, W. Wei, B. Peng and W. Sun, *Materials*, 2019, **12**, 3641.
21 L. Zeng, D. Yang, Z. Li, W. Xiong, M. Hao, H. Ma, H. Yuan and J. Cui, *Ceram. Int.*, 2024, **50**, 19402–19411.
22 R. N. Perumal and V. Athikesavan, *Ferroelectrics*, 2020, **555**, 88–100.
23 G. Nag Bhargavi, T. Badapanda, A. Khare, M. Shahid Anwar and N. Brahme, *Appl. Phys. A*, 2021, **127**, 1–18.
24 F. Bahri and H. Khemakhem, *J. Alloys Compd.*, 2014, **593**, 202–206.
25 P. Kumar Patel and K. L. Yadav, *Phys. B*, 2014, **442**, 39–43.
26 K. Zhang, T. Li and Y. Xu, *Materials*, 2023, **16**, 6635.
27 T. Badapanda, L. S. Cavalcante, G. E. da Luz, N. C. Batista, S. Anwar and E. Longo, *Metall. Mater. Trans. A*, 2013, **44**, 4296–4309.
28 F. Benabdallah, A. Simon, H. Khemakhem, C. Elissalde and M. Maglione, *J. Appl. Phys.*, 2011, **109**, 124116.
29 A. Dahri, Y. Gagou, N. Abdelmoula, H. Khemakhem and M. El Marssi, *Ceram. Int.*, 2022, **48**, 3157–3171.
30 V. S. Puli, D. K. Pradhan, D. B. Chrisey, M. Tomozawa, G. L. Sharma, J. F. Scott and R. S. Katiyar, *J. Mater. Sci.*, 2013, **48**, 2151–2157.
31 A. R. Jayakrishnan, K. V. Alex, A. Thomas, J. P. B. Silva, K. Kamakshi, N. Dabra, K. C. Sekhar, J. Agostinho Moreira and M. J. M. Gomes, *Ceram. Int.*, 2019, **45**, 5808–5818.
32 Y. Zhou, Q. Lin, W. Liu and D. Wang, *RSC Adv.*, 2016, **6**, 14084–14089.
33 A. Bendahhou, K. Chourti, M. Loutou, S. El Barkany and M. Abou-Salama, *RSC Adv.*, 2022, **12**, 10895–10910.
34 K. Aliouane, A. Guehria-Laidoudi, A. Simon and J. Ravez, *Solid State Sci.*, 2005, **7**, 1324–1332.
35 T. Badapanda, S. Sarangi, B. Behera, S. Anwar, T. Sinha, R. Ranjan, G. Luz, E. Longo and L. Cavalcante, *J. Mater. Sci.: Mater. Electron.*, 2014, **25**, 3427–3439.
36 G. N. Bhargavi, A. Khare, T. Badapanda and M. S. Anwar, *Appl. Phys. A*, 2018, **124**, 1–9.
37 S. Lenka, T. Badapanda, P. Nayak, S. Sarangi and S. Anwar, *Ceram. Int.*, 2021, **47**, 5477–5486.
38 N. Rhimi, N. Dhahri, M. Khelifi, E. K. Hlil and J. Dhahri, *Inorg. Chem. Commun.*, 2022, **146**, 110119.
39 C. Ostos, L. Mestres, M. Martínez-Sarrión, J. Garcia, A. Albareda and R. Perez, *Solid State Sci.*, 2009, **11**, 1016–1022.
40 E. Hassan Yahakoub, A. Bendahhou, F. Chaou, I. Jalafi, S. E. L. Barkany, Z. Bahari and M. Abou-Salama, *Ceram. Int.*, 2024, **50**, 19002–19016.
41 V. Petříček, M. Dušek and L. Palatinus, *Z. Kristallogr. - Cryst. Mater.*, 2014, **229**, 345–352.
42 W. Zhu, Z.-Y. Shen, W. Deng, K. Li, W. Luo, F. Song, X. Zeng, Z. Wang and Y. Li, *J. Materiomics*, 2024, **10**, 86–123.
43 F. Chaou, I. Jalafi, A. Bendahhou, E. H. Yahakoub, S. El Barkany and M. Abou-Salama, *Mater. Chem. Phys.*, 2023, **310**, 128426.
44 S. Mahajan, O. Thakur, C. Prakash and K. Sreenivas, *Bull. Mater. Sci.*, 2011, **34**, 1483–1489.
45 W. Cai, Q. Zhang, C. Zhou, R. Gao, F. Wang, G. Chen, X. Deng, Z. Wang, N. Deng, L. Cheng and C. Fu, *J. Mater. Sci.*, 2020, **55**, 9972–9992.
46 Y. Tian, L. Wei, X. Chao, Z. Liu and Z. Yang, *J. Am. Ceram. Soc.*, 2013, **96**, 496–502.
47 M. Sindhu, N. Ahlawat, S. Sanghi, R. Kumari and A. Agarwal, *J. Alloys Compd.*, 2013, **575**, 109–114.
48 A. Hota, T. Badapanda, S. K. Rout and S. B, *Chem. Phys. Impact*, 2023, **7**, 100304.
49 S. B. Reddy, K. P. Rao and M. R. Rao, *J. Alloys Compd.*, 2011, **509**, 1266–1270.
50 L. T. H. Phong, N. T. Dang, N. V. Dang, V.-Q. Nguyen, D. H. Manh, P. H. Nam, L. H. Nguyen and P. T. Phong, *RSC Adv.*, 2022, **12**, 16119–16130.
51 K. Siemek, A. Olejniczak, L. N. Korotkov, P. Konieczny and A. V. Belushkin, *Appl. Surf. Sci.*, 2022, **578**, 151807.
52 W. Huang, X. Du, S. K. Thatikonda, N. Qin, C. Yao, A. Hao and D. Bao, *Ceram. Int.*, 2019, **45**, 10475–10480.
53 M. B. Bechir, A. Almeshal and M. H. Dhaou, *Mater. Res. Bull.*, 2023, **157**, 112012.

54 A. Bendahhou, E. H. Yahakoub, K. Lemrini, T. Moudrikah, S. Raissi, E. H. Lahrar, R. E. Malekshah, F. Chaou, I. Jalafi, K. Chourti, M. El Miz, S. El Barkany and M. Abou-Salama, *J. Alloys Compd.*, 2025, **1020**, 179356.
55 F. Chaou, I. Jalafi, A. Chrir, E. H. Yahakoub, K. Chourti, A. Bendahhou, S. El Barkany, P. Marchet and M. Abou-Salama, *Ceram. Int.*, 2024, **50**, 31135–31146.
56 S. M. L. S, S. Bhaskar, R. Dahiwadkar, S. Kanvah, S. S. Ramamurthy, S. Bhaktha and B. N, *ACS Appl. Nano Mater.*, 2023, **6**, 19312–19326.
57 D. Jing, L. Guo, L. Zhao, X. Zhang, H. Liu, M. Li, S. Shen, G. Liu, X. Hu, X. Zhang, K. Zhang, L. Ma and P. Guo, *Int. J. Hydrogen Energy*, 2010, **35**, 7087–7097.
58 M. Fahad, R. Thangavel and P. Sarun, *Mater. Sci. Eng., B*, 2022, **283**, 115837.
59 M. B. Smith, K. Page, T. Siegrist, P. L. Redmond, E. C. Walter, R. Seshadri, L. E. Brus and M. L. Steigerwald, *J. Am. Chem. Soc.*, 2008, **130**, 6955–6963.
60 Y. Niu, F. Zhang, X. Zhang, Z. Zhang, Y. Bai and Z. J. Wang, *Ceram. Int.*, 2024, **50**, 230–237.
61 X. Tang, K.-H. Chew and H. Chan, *Acta Mater.*, 2004, **52**, 5177–5183.
62 F. Chaou, A. Bendahhou, K. Chourti, I. Jalafi, E. H. Yahakoub, S. El Barkany and M. Abou-Salama, *Ceram. Int.*, 2023, **49**, 17940–17952.
63 Z. Guo, Q. Zhu, S. Wu, C. Hu, L. Liu and L. Fang, *Ceram. Int.*, 2018, **44**, 7700–7708.
64 X. Diez-Betriu, J. Garcia, C. Ostos, A. Boya, D. Ochoa, L. Mestres and R. Perez, *Mater. Chem. Phys.*, 2011, **125**, 493–499.
65 A. B. J. Kharrat, M. Bourouina, N. Moutia, K. Khirouni and W. Boujelben, *J. Alloys Compd.*, 2018, **741**, 723–733.
66 A. R. Jayakrishnan, J. P. B. Silva, K. Kamakshi, D. Dastan, V. Annapureddy, M. Pereira and K. C. Sekhar, *Prog. Mater. Sci.*, 2023, **132**, 101046.
67 X. G. Tang, J. Wang, X. X. Wang and H. L. W. Chan, *Solid State Commun.*, 2004, **131**, 163–168.
68 P. R. Das, L. Biswal, B. Behera and R. N. P. Choudhary, *Mater. Res. Bull.*, 2009, **44**, 1214–1218.
69 K. A. Hunnestad, E. D. Roede, A. T. J. van Helvoort and D. Meier, *J. Appl. Phys.*, 2020, **128**, 191102.
70 R. Sarkar, B. Sarkar and S. Pal, *Appl. Phys. A*, 2021, **127**, 177.
71 E. H. Yahakoub, A. Bendahhou, I. Jalafi, F. Chaou, S. El Barkany, Z. Bahari and M. Abou-Salama, *Heliyon*, 2023, **9**, e21037.
72 A. Bendahhou, K. Chourti, E. H. Yahakoub, F. Chaou, I. Jalafi, S. E. Barkany and M. Abou-Salama, *Mater. Res. Bull.*, 2023, **165**, 112319.
73 A. Bendahhou, P. Marchet, S. El Barkany and M. Abou-Salama, *J. Alloys Compd.*, 2021, **882**, 160716.
74 T. Badapanda, S. Sarangi, B. Behera, S. Anwar, T. Sinha, R. Ranjan, G. Luz, E. Longo and L. Cavalcante, *J. Mater. Sci.: Mater. Electron.*, 2014, **25**, 3427–3439.
75 I. Jalafi, A. Bendahhou, K. Chourti, F. Chaou, E. Hassan Yahakoub, S. E. L. Barkany and M. Abou-Salama, *Ceram. Int.*, 2023, **49**, 10213–10223.
76 I. Jalafi, F. Chaou, K. Chourti, M. Chokri, W. El Hadouchi, E. H. Yahakoub, A. Bendahhou, S. El Barkany and M. Abou-Salama, *Ceram. Int.*, 2025, **51**, 17547–17556.
77 S. Wu, C. Sun, X. Yang, C. Hu, L. Liu and L. Fang, *Ceram. Int.*, 2020, **46**, 9240–9248.
78 L. Liu, M. Wu, Y. Huang, Z. Yang, L. Fang and C. Hu, *Mater. Chem. Phys.*, 2011, **126**, 769–772.
79 O. Raymond, R. Font, J. Portelles, N. Suárez-Almodovar and J. M. Siqueiros, *J. Appl. Phys.*, 2006, **99**, 124101.
80 K. N. D. K. Muhsen, R. A. M. Osman and M. S. Idris, *J. Mater. Sci.: Mater. Electron.*, 2019, **30**, 20673–20686.
81 S. Brahma, R. Choudhary and A. K. Thakur, *Phys. B*, 2005, **355**, 188–201.
82 K. Parida, S. K. Dehury and R. Choudhary, *Mater. Sci. Eng., B*, 2017, **225**, 173–181.
83 S. K. Barik, R. Choudhary and A. Singh, *Adv. Mater. Lett.*, 2011, **2**, 419–424.
84 A. Bendahhou, K. Chourti, R. El Bouayadi, S. El Barkany and M. Abou-Salama, *RSC Adv.*, 2020, **10**, 28007–28018.
85 R. Gerhardt, *J. Phys. Chem. Solids*, 1994, **55**, 1491–1506.
86 J. Liu, C.-G. Duan, W.-G. Yin, W.-N. Mei, R. W. Smith and J. R. Hardy, *J. Chem. Phys.*, 2003, **119**, 2812–2819.
87 S. Madolappa, B. Ponraj, R. Bhimireddi and K. B. Varma, *J. Am. Ceram. Soc.*, 2017, **100**, 2641–2650.
88 S. Madolappa, H. K. Choudhary, N. Punia, A. Anupama and B. Sahoo, *Mater. Chem. Phys.*, 2021, **270**, 124849.
89 R. Bergman, *J. Appl. Phys.*, 2000, **88**, 1356–1365.